รายงานวิจัยฉบับสมบูรณ์

โครงการ โครงสร้างทางอิเล็กทรอนิกส์บนพื้นผิวและภายในก้อนสารของสตรอนเทียมไททาเนต: ตัวนำไฟฟ้ายิ่งยวดและตัวกำเนิดชั้นอิเล็กตรอนสองมิติ

โดย ดร. วรวัฒน์ มีวาสนา

เดือน ปี ที่เสร็จโครงการ

6/2555

สัญญาเลขที่ MRG5380032

รายงานวิจัยฉบับสมบูรณ์

โครงการ โครงสร้างทางอิเล็กทรอนิกส์บนพื้นผิวและภายในก้อนสารของสตรอนเทียมไททาเนต: ตัวนำไฟฟ้ายิ่งยวดและตัวกำเนิดชั้นอิเล็กตรอนสองมิติ

ผู้วิจัย ดร. วรวัฒน์ มีวาสนา
สังกัด สาขาวิชาฟิสิกส์ มหาวิทยาลัยเทคโนโลยีสุรนารี

สนับสนุนโดยสำนักงานกองทุนสนับสนุนการวิจัย

บทคัดย่อ

รหัสโครงการ : MRG5380032

ชื่อโครงการ : โครงสร้างทางอิเล็กทรอนิกส์บนพื้นผิวและภายในก้อนสารของสตรอนเทียมไททาเนต: ตัวนำไฟฟ้ายิ่งยวดและตัวกำเนิดชั้นอิเล็กตรอนสองมิติ

ชื่อนักวิจัย : ดร. วรวัฒน์ มีวาสนา สังกัด สาขาวิชาฟิสิกส์ มหาวิทยาลัยเทคโนโลยีสุรนารี

E-mail Address : worawat@g.sut.ac.th

ระยะเวลาโครงการ : 2 ปี

งานวิจัยนี้เป็นการศึกษาสารประกอบสตรอนเทียมไททาเนต ($SrTiO_3$) ซึ่งมีสมบัติในก้อนสาร (Bulk property) ทางไฟฟ้าที่หลากหลาย สตรอนเทียมไททาเนตเป็นสารประกอบที่มีค่าคงที่ไดอิเล็กตริก (Static dielectric constant) ที่สูงถึงหลักหมื่นที่อุณหภูมิต่ำ และเป็นสารประกอบโลหะออกไซด์ที่ถูกค้นพบเป็นสารแรกว่าสามารถนำไฟฟ้ายวดยิ่งได้ ในปี ค.ศ. 2004 มีการค้นพบว่าที่บริเวณผิวสัมผัสของสารประกอบนี้กับอะลูมิเนียมออกไซด์ $LaAlO_3$ จะมีชั้นอิเล็กตรอนสองมิติที่มีสมบัติเฉพาะตัวทางแม่เหล็กไฟฟ้าที่หลากหลายกว่าในสารกึ่งตัวนำแบบดั้งเดิม ข้าพเจ้าและคณะจึงได้ทำการศึกษาโครงสร้างทางอิเล็กทรอนิกส์ของสตรอนเทียมไททาเนตทั้งภายในก้อนสาร (Bulk) และเฉพาะบนพื้นผิว (Surface) โดยใช้เทคนิคโฟโตอิมิชชันแบบแยกแยะเชิงมุมรวมถึงการวัดความต้านทานของพื้นผิวซึ่งมีการทดลองทั้งในและต่างประเทศ

จากการศึกษาโครงสร้างทางอิเล็กทรอนิกส์ภายในก้อนสารที่มีการโดปประมาณ 1% และ5% พบว่าโครงสร้างโดยรวมสอดคล้องกับการคำนวณ แต่สำหรับอันตรกิริยาระหว่างอิเล็กตรอนและโฟนอน คณะวิจัยกลับพบว่ามีความแรงแค่ระดับกลางซึ่งผิดความคาดหมาย ข้อมูลดังกล่าวได้ใช้เป็นตัวบ่งบอกถึงลักษณะที่แตกต่างกันระหว่างอันตรกิริยาระหว่างอิเล็กตรอนและโฟนอนในตัวฉนวนทั่วไปและตัวฉนวนแบบมอตต์ (Mott insulator) ได้ดี และจากการศึกษาโครงสร้างทางอิเล็กทรอนิกส์บนพื้นผิว พบว่าบนผิวของผลึกสตรอนเทียมไททาเนตสามารถมีเกิดชั้นอิเล็กตรอนสองมิติได้หลังจากการฉายแสงซินโครตรอนที่มีความเข้มสูงโดยความหนาแน่นอิเล็กตรอนยังสามารถเปลี่ยนได้ตามค่าโดสที่เปลี่ยนไป วิธีการดังกล่าวอาจใช้เป็นวิธีในการสร้างลวดลายของชั้นอิเล็กตรอนในวงจรไฟฟ้าแบบใหม่ที่ราคาถูกและรวดเร็วได้ นอกจากนี้ยังพบว่าอิเล็กตรอนที่ถูกขังในชั้นอิเล็กตรอนสองมิตินี้ มีอันตรกิริยาของอิเล็กตรอนสูงแต่กลับมีความคล่องตัวที่สูงด้วยซึ่งเป็นที่น่าศึกษาต่อในเชิงทฤษฎี และหาทางประยุกต์ใช้ในการสร้างอุปกรณ์อิเล็กทรอนิกส์แบบใหม่ นอกจากนี้ยังมีงานวิจัยอีก 2 เรื่องเกี่ยวกับสารประกอบคอปเปอร์ออกไซด์ และกราฟีนที่ได้รับการสนับสนุนบางส่วนจากทุนนี้

คำหลัก : สตรอนเทียมไททาเนต โครงสร้างทางอิเล็กทรอนิกส์ เทคนิคโฟโตอิมิชชันแบบแยกแยะเชิงมุม อันตรกิริยาระหว่างอิเล็กตรอนและโฟนอน และชั้นอิเล็กตรอนสองมิติ

Abstract

Project Code : MRG5380032

Project Title : Surface and Bulk Electronic Structure of Strontium Titanate, SrTiO3: the Classic Superconductor and the New 2D-Electron-Layer Host

Investigator : Dr. Worawat Meevasana, School of Physics, Suranaree University of Technology

E-mail Address : worawat@g.sut.ac.th

Project Period : 2 years

Here we are interested strontium titanate ($SrTiO_3$) which has many bulk properties such as high dielectric constant (e.g. in order of 10,000 at low temperature) and exhibits superconducting state (which was discovered for the first time, among oxides). In 2004, it was discovered that two-dimensional electron gas (2DEG) could occur at the interface between $SrTiO_3$ and $LaAlO_3$. This 2DEG displays novel electrical and magnetic properties beyond conventional semiconductors. In trying to understand these properties, we therefore study both the surface and bulk electronic structures of $SrTiO_3$ by using angle-resolved photoemission spectroscopy and also the surface electrical conductivity; the experiments were performed both in Thailand and aboard.

From the measured bulk electronic structures of 1% and 5%-doped samples, we found that they are mostly in agreement with the calculation, except the unexpected moderate coupling between electrons and phonons (el-ph coupling). This finding helps highlighting the difference of el-ph coupling between band and Mott insulators. From the surface electronic structure, we find that 2DEG states could occur at the bare surface of $SrTiO_3$ under intense synchrotron light; the electron density could also be varied by applying different irradiation doses. This method may be used as a fast and inexpensive way to create 2DEG pattern in new-generation electronic devices. Besides this, we also found that surprisingly both signature of strong interactions and light effective mass coexisted; this interesting coexistence should be subjected for further investigation. Additional to these studies, there are also the other two studies: copper-oxide and graphene which were partially funded by this grant.

Keywords : Strontium titanate, electronic structure, angle-resolved photoemission spectroscopy, electron-phonon coupling, and two-dimensional electron gas.

วัตถุประสงค์

เพื่อศึกษาโครงสร้างทางอิเล็กทรอนิกส์ของสตรอนเทียมไททาเนตทั้งบนพื้นผิว (สองมิติ) และภายในก้อนสาร (สามมิติ) โดยใช้เทคนิคโฟโตอิมิชชันแบบแยกแยะเชิงมุม

วิธีทดลอง

ก. ขั้นตอนการเตรียมสารสตรอนเทียมไททาเนต

เลือกผลึกสตรอนเทียมไททาเนตที่มีสารเจือของธาตุ La (แทนที่ธาตุ Sr) ที่มีความเข้มข้นต่ำเพื่อให้นำไฟฟ้าเพียงเล็กน้อยเพื่อสะดวกต่อการทดลองโฟโตอิมิชชัน ทดสอบโดยการวัดความต้านทาน ถ้าไม่ทราบระนาบของผลึกอาจจะต้องวัดระนาบของผลึกด้วยเครื่อง X-ray Diffraction แบบ Laue ในการทดลองโฟโตอิมิชชันต้องการความสะอาดสูงมาก วิธีหนึ่งที่ใช้ทั่วไปคือการทำให้ผลึกแตกออกในสุญญากาศเพื่อได้พื้นผิวที่สะอาด เพื่อที่ผลึกแตกออกอย่างราบเรียบ ก่อนนำผลึกไปวัดเทคนิคที่สำคัญคือการตัดผลึกบางส่วนในแนวที่ผลึกจะแตกออก การตัดนำร่องนี้ต้องอาศัยเครื่องตัดผลึกแบบเส้นลวด หลังจากการตัดนำร่องต้องล้างผลึกให้สะอาดด้วยแอลกอฮอล์ก่อนใส่เข้าสู่ระบบสุญญากาศในเครื่องโฟโตอิมิชชัน

ข. ขั้นตอนการวัดโครงสร้างทางอิเล็กทรอนิกส์โดยเทคนิคโฟโตอิมิชชันแบบแยกแยะเชิงมุม

สำหรับโครงการนี้จะเลือกอุณหภูมิสองช่วงคืออุณหภูมิห้อง และอุณหภูมิประมาณ 20 เคลวินโดยใช้ฮีเลียมเหลวในการควบคุมอุณหภูมิ หลังจากปรับอุณหภูมิให้เท่ากับอุณหภูมิที่จะศึกษาแล้วทำผลึกให้แตกออก สามารถตรวจสอบความเรียบได้โดยการฉายแสงเลเซอร์เพื่อดูภาพสะท้อน หลังจากนั้นทำการวัดโครงสร้างทางอิเล็กทรอนิกส์ โดยฉายแสงยูวีที่มีความเข้มสูงจากเครื่องซินโครตรอนที่พลังงานโฟตอนระหว่าง 40-80 eV ซึ่งการฉายแสงดังกล่าวยังทำให้เกิดชั้นอิเล็กตรอนสองมิติขึ้นด้วยซึ่งอยู่รวมกับโครงสร้างอิเล็กตรอนในก้อนสาร จากนั้นวัดสเปกตรัมความหนาแน่นของโฟโตอิเล็กตรอนที่หลุดออกมาเป็นฟังก์ชันของพลังงาน เปลี่ยนไปวัดที่ค่ามุมต่าง ๆเพื่อเป็นการแยกแยะเชิงมุมเพื่อดูการกระจายตัวที่ค่าโมเมนตัมต่าง ๆซึ่งจะเป็นข้อมูลสำคัญในโครงการนี้ ทำการตรวจสอบหาโครงสร้างอะตอมที่พื้นผิวโดยการใช้เครื่อง Low Energy Electron Diffraction (LEED)

หมายเหตุ นอกจากการวัดผลึกสตรอนเทียมไททาเนต ข้าพเจ้ายังได้ศึกษาสารประกอบคอปเปอร์ออกไซด์และกราฟีนด้วย

ค. ขั้นตอนการวัดต้านทานไฟฟ้าบนพื้นผิวหลังการฉายแสงยูวี

นำสารตัวอย่างเข้าสู่ระบบสุญญากาศซึ่งเป็นการเพิ่มประสิทธิภาพของการฉายแสง เนื่องจากแสงยูวีจะถูกดูดกลืนได้ง่ายในอากาศปกติทำให้ความเข้มลดลง หลังจากความดันอากาศอยู่ในช่วงต่ำกว่า 10^{-7} torr จะทำการตรวจสอบสภาพนำไฟฟ้าบนผิวโดยการวัดความต้านทานก่อนฉายแสง ต่อจากนั้นฉายแสงบนสารตัวอย่างด้วยแสงยูวีที่ปรับ ความเข้มแสง

พลังงาน และขนาดของลำแสงให้มีค่าตามที่ต้องการ แล้วจึงตรวจสอบสภาพนำไฟฟ้าบนผิว โดยการวัดความต้านทานหลังฉายแสงอีกครั้ง

ง. ขั้นตอนการวิเคราะห์ผลและการเปรียบเทียบผลที่ได้กับการคำนวณ

ใช้โปรแกรม Igor ของบริษัท Wavematrics ในการวิเคราะห์ผลการทดลองเพื่อดูโครงสร้างทางอิเล็กทรอนิกส์โดยเฉพาะการกระจายตัวของอิเล็กตรอนในฟังก์ชั่นของพลังงานและโมเมนตัม หรือ Electron band dispersion ในช่วงพลังงานใกล้กับชั้นพลังงานเฟอร์มิ (ประมาณ 0-300 meV) เปรียบเทียบกับโครงสร้างอิเล็กทรอนิกส์ที่ได้จากการคำนวณโดยวิธี Local Density Approximation ที่มีอยู่แล้ว หรือผลการคำนวณเพิ่มเติมจากนักวิจัยร่วม และทำการเปรียบเทียบกับผลการทดลองจากเทคนิคอื่นเช่น ค่ามวลประสิทธิ (Effective mass) ของอิเล็กตรอนจากค่าความต้านทาน หรือจากสมบัติทางแสงเพื่อเป็นการยืนยัน หรือในกรณีที่ผลการทดลองไม่ตรงกับผลการคำนวณ ข้อมูลส่วนที่ต่างกันนี้อาจจะช่วยบ่งบอกถึงที่มาของการกำเนิดสมบัติโดดเด่นของสตรอนเทียมไททาเนตที่กล่าวมาข้างต้นได้

ผลการทดลอง

1. การศึกษาโครงสร้างทางอิเล็กทรอนิกส์ภายในก้อนสารผลึกสตรอนเทียมไททาเนต

จากการศึกษาโครงสร้างทางอิเล็กทรอนิกส์ภายในก้อนสารผลึกสตรอนเทียมไททาเนตที่มีสารเจือของธาตุ La ประมาณ 1% และ5% พบว่าโครงสร้างตามรูปที่ 1 โดยรวมมีผลที่สอดคล้องกับการคำนวณด้วยวิธี Local Density Approximation (LDA) แต่สำหรับอันตรกิริยาระหว่างอิเล็กตรอนและโฟนอน คณะวิจัยกลับพบว่ามีความแรงแค่ระดับกลางซึ่งผิดความคาดหมาย ข้อมูลดังกล่าวได้ใช้เป็นตัวบ่งบอกถึงลักษณะที่แตกต่างกันระหว่างอันตรกิริยาระหว่างอิเล็กตรอนและโฟนอนในตัวฉนวนทั่วไปและตัวฉนวนแบบมอตต์ (Mott insulator) ได้ดีตามตารางที่ 1

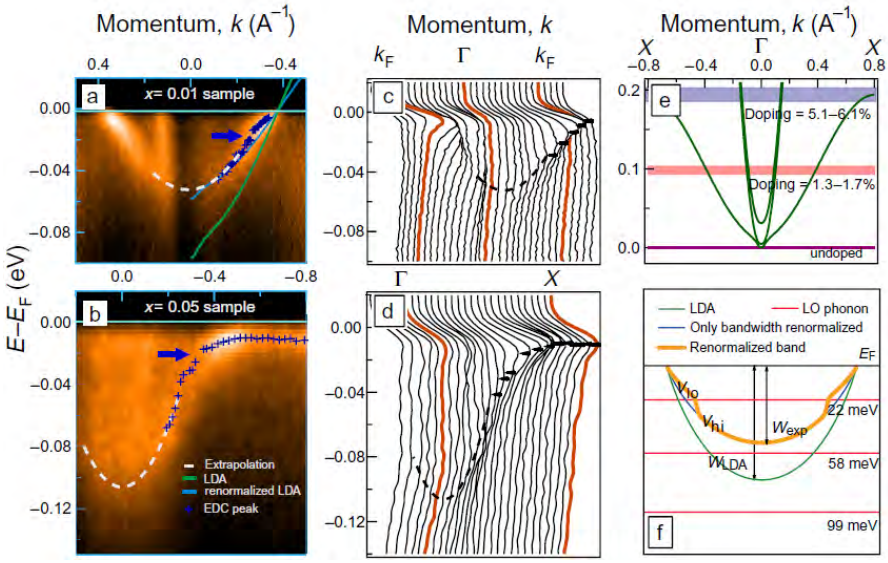

รูปที่ 1 โครงสร้างทางอิเล็กทรอนิกส์ภายในก้อนสารผลึกสตรอนเทียมไททาเนตที่มีสารเจือของธาตุ La ประมาณ 1% และ5% (เอกสารที่ 4 ในภาคผนวก)

Feature	Mott insulator (La_2CuO_4)	Band insulator (STO)
Mass renormalization factor from the kink feature at small doping $x = 0.01$	~3.7	~1.3
Small polaronic effect at small doping	Yes	No
Large pseudogap behavior at small doping	Yes	No
Small Fermi surface pocket at small doping	Maybe (YBCO) [27]	Yes
Dielectric constant (undoped)	~20 [28]	$\sim 10^2 - 10^4$

ตารางที่ 1 การเปรียบเทียบลักษณะโครงสร้างอิเล็กทรอนิกส์ต่าง ๆ ระหว่างตัวฉนวนแบบทั่วไป (Band insulator) กับตัวฉนวนแบบมอตต์ (Mott insulator)

2. การศึกษาโครงสร้างทางอิเล็กทรอนิกส์ภายในก้อนสารผลึกสตรอนเทียมไททาเนต

จากการศึกษาโครงสร้างทางอิเล็กทรอนิกส์บนพื้นผิว พบว่าบนผิวของผลึกสตรอนเทียมไททาเนตสามารถมีเกิดชั้นอิเล็กตรอนสองมิติได้หลังจากการฉายแสงซินโครตรอนที่มีความเข้มสูงโดยความหนาแน่นอิเล็กตรอนยังสามารถเปลี่ยนได้ตามค่าโดสที่เปลี่ยนไปตามรูปที่ 2 วิธีการดังกล่าวอาจใช้เป็นวิธีในการสร้างลวดลายของชั้นอิเล็กตรอนในวงจรไฟฟ้าแบบใหม่ที่ราคาถูกและรวดเร็วได้ นอกจากนี้ยังพบว่าอิเล็กตรอนที่ถูกขังในชั้นอิเล็กตรอนสองมิตินี้มีอันตรกิริยาของอิเล็กตรอนสูงตามการเปรียบเทียบในรูปที่ 3 อย่างแต่กลับมีความคล่องตัวที่สูงด้วยซึ่งเป็นเรื่องที่แปลกและน่าศึกษาต่อในเชิงทฤษฎีต่อไป

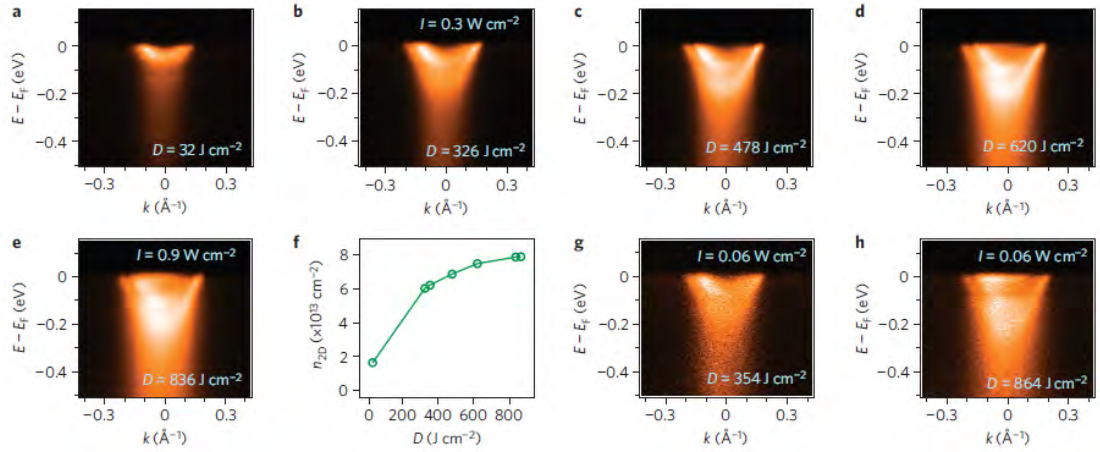

รูปที่ 2 โครงสร้างทางอิเล็กทรอนิกส์ของชั้นอิเล็กตรอนสองมิติบนผิวสารผลึกสตรอนเทียมไททาเนตโดยความหนาแน่นอิเล็กตรอนเปลี่ยนค่าได้ตามปริมาณโดสของแสงที่ฉายลงไป (เอกสารที่ 1 ในภาคผนวก)

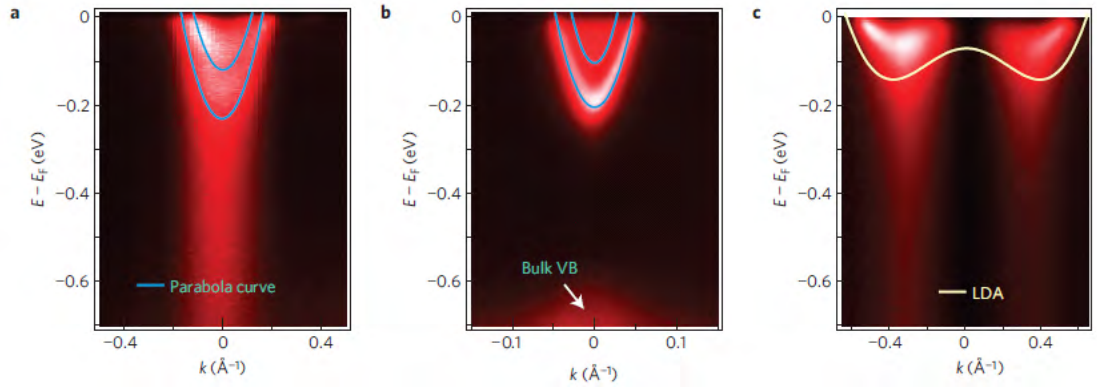

รูปที่ 3 การเปรียบเทียบโครงสร้างทางอิเล็กทรอนิกส์ของชั้นอิเล็กตรอนสองมิติบนผิวของ (a) สารผลึกสตรอนเทียมไททาเนต (b) สารกึ่งตัวนำ InAs และ (c) โครงสร้างทางอิเล็กทรอนิกส์ของตัวนำไฟฟ้ายวดยิ่งอุณหภูมิวิกฤตสูง

3. การศึกษาโครงสร้างทางอิเล็กทรอนิกส์ของสารประกอบคอปเปอร์ออกไซด์

ต่อเนื่องจากการค้นพบโครงสร้างทางอิเล็กทรอนิกส์แบบใหม่ของตัวนำไฟฟ้ายวดยิ่งอุณหภูมิวิกฤตสูง (สารประกอบคอปเปอร์ออกไซด์) โดยโครงสร้างนี้มีลักษณะเป็นวงปิด (Electron pocket) ทางคณะวิจัยของข้าพเจ้าได้พบว่าลักษณะดังกล่าวเกิดขึ้นจากโครงสร้างทางอะตอมที่บิดเบี้ยวต่อ ๆกันซึ่งเรียกว่า Superlattice ตามรูปที่ 4

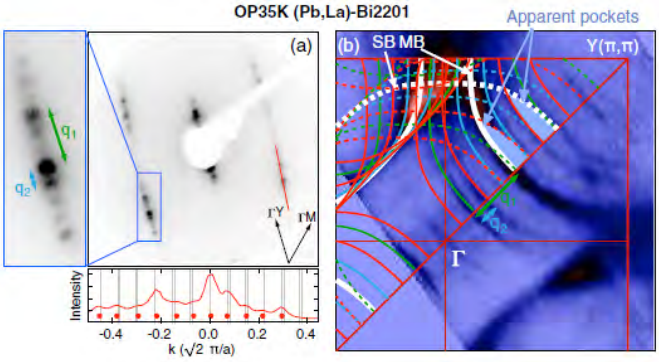

รูปที่ 4 โครงสร้างทางอิเล็กทรอนิกส์ของสารประกอบคอปเปอร์ออกไซด์ (Bi2201) และการดูโครงสร้างอะตอมที่พื้นผิวโดยการใช้เทคนิค Low Energy Electron Diffraction (LEED) (เอกสารที่ 2 ในภาคผนวก)

4. การศึกษาจำนวนชั้นกราฟีนบนผิวของผลึก SiC ที่มีรอยขูดขีด

จากการนับจำนวนชั้นกราฟีนบนผิวของผลึก SiC ที่มีรอยขูดขีดด้วยเทคนิค Low energy electron microscopy/spectroscopy พบว่าจำนวนชั้นกราฟีนที่ใกล้กับรอยขูดขีดมีความหนากว่าและขยายตัวออกห่างจากรอยขูดขีดเป็นระยะหนึ่งด้วยตามรูปที่ 5

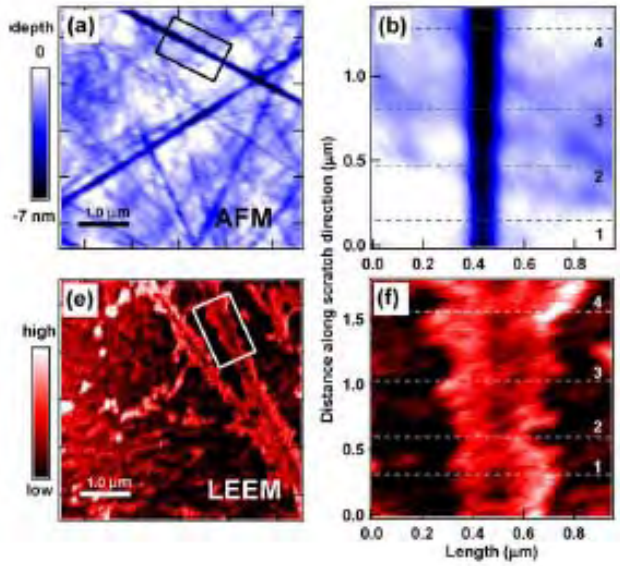

รูปที่ 5 การศึกษาชั้นกราฟีนบนผิวของผลึก SiC ก่อนและหลังการปลูกด้วยเทคนิค Low energy electron microscopy (LEEM) และ Atomic force microscopy (AFM) (เอกสารที่ 3 ในภาคผนวก)

สรุปและวิจารณ์ผลการทดลอง

การวิจัยในโครงการนี้บรรลุผลตามวัตถุประสงค์ซึ่งเป็นศึกษาโครงสร้างทางอิเล็กทรอนิกส์ของสตรอนเทียมไททาเนตทั้งบนพื้นผิว (สองมิติ) และ ภายในก้อนสาร (สามมิติ) ซึ่งก่อให้เกิดความรู้ทั้งเรื่องอันตรกิริยาระหว่างอิเล็กตรอนและโฟนอนจากโครงสร้างภายในก้อนสาร รวมทั้งการค้นพบชั้นอิเล็กตรอนสองมิติที่มีสมบัติโดดเด่นเทียบกับของสารกึ่งตัวแบบดังเดิม

ทั้งนี้ยังได้มีโอกาสศึกษาเพิ่มเติมตามแผนการดำเนินงานข้อ 7 (ของข้อเสนอโครงการ) ในหัวข้ออื่นๆ ซึ่งเป็นเรื่องเกี่ยวกับตัวนำไฟฟ้ายวดยิ่งอุณหภูมิวิกฤตสูง (สารประกอบคอปเปอร์ออกไซด์) และการเกิดชั้นกราฟีนที่แตกต่างกันบนผิวของผลึก SiC

ข้อเสนอแนะสำหรับงานวิจัยในอนาคต

การค้นพบชั้นอิเล็กตรอนสองมิติบนผิวของสตรอนเทียมไททาเนตที่เกิดจากการฉายแสงยูวีเป็นเรื่องที่น่าสนใจ ซึ่งวิธีการดังกล่าวอาจใช้เป็นวิธีในการสร้างลวดลายของชั้นอิเล็กตรอนในวงจรไฟฟ้าแบบใหม่ที่ราคาถูกและรวดเร็วได้ คณะวิจัยเห็นว่าน่าจะมีการทดลองสร้างวงไฟฟ้าแบบง่ายด้วยวิธีดังกล่าว หรืออุปกรณ์ทางไฟฟ้า เช่น เซ็นเซอร์แสง (ซึ่งได้เริ่มทำการทดลองไปแล้วไปบางส่วน สามารถอ่านเพิ่มได้จาก เอกสารที่ 5 ในภาคผนวก)

Output จากโครงการวิจัยที่ได้รับทุนจาก สกว.

1. ผลงานตีพิมพ์ในวารสารวิชาการนานาชาติ (ระบุชื่อผู้แต่ง ชื่อเรื่อง ชื่อวารสาร ปี เล่มที่ เลขที่ และหน้า) หรือผลงานตามที่คาดไว้ในสัญญาโครงการ

   1.1 **W. Meevasana**, P. D. C. King, R. H. He, S-K. Mo, M. Hashimoto, A. Tamai, P. Songsiriritthigul, F. Baumberger and Z-X. Shen, "Creation and control of a two-dimensional electron liquid at the bare $SrTiO_3$ surface", *Nature Materials* 10, 114-118 (2011) เอกสารที่ 1 ในภาคผนวก

   1.2 P.D.C.King, J.A. Rosen, **W. Meevasana**, A. Tamai, E. Rozbicki, R. Comin, G. Levy, D. Fournier, Y. Yoshida, H. Eisaki, K.M. Shen, N.J.C. Ingle, A. Damascelli, F. Baumberger, "Structural origin of apparent Fermi surface pockets in angle-resolved photoemission of $Bi_2Sr_{2-x}La_xCuO_6$", *Physical Review Letters* 106, 127005 (2011) เอกสารที่ 2 ในภาคผนวก

   1.3 J. Osaklunga, C.Euaruksakul, **W.Meevasana***, P.Songsiriritthigul, "Spatial variation of the number of graphene layers formed on the scratched 6H–SiC(0001) surface", *Applied Surface Science* 258, 4672-4677 (2012) เอกสารที่ 3 ในภาคผนวก

   หมายเหตุ ผลงานที่เกี่ยวข้องซึ่งมี สกว. ในกิตติกรรมประกาศ แต่ไม่ขอนำมานับรวมในการปิดโครงการนี้

   W. Meevasana*, X.J. Zhou, B. Moritz, C.-C. Chen, R.H. He, S.-I. Fujimori, D.H. Lu, S.-K. Mo, R.G. Moore, F. Baumberger, T.P. Devereaux, D. Van Der Marel, N. Nagaosa, J. Zaanen, Z.-X. Shen, "Strong energy-momentum dispersion of phonon-dressed carriers in the lightly doped band insulator $SrTiO_3$", *New Journal of Physics* 12, 23004 (2010) เอกสารที่ 4 ในภาคผนวก

2. การนำผลงานวิจัยไปใช้ประโยชน์

   -ไม่มี-

3. อื่นๆ (เช่น ผลงานตีพิมพ์ในวารสารวิชาการในประเทศ การเสนอผลงานในที่ประชุมวิชาการ หนังสือ การจดสิทธิบัตร)

3.1 S. Suwanwong, T. Eknapakul, C. Masingboon, P. Buaphet, S. Rattanasuporn, R. Pattanakul, H. Nakajima and **W. Meevasana***, "UV Irradiation Effect on Electrical Conductivity of $KTaO_3$ Crystals", *Proceedings of Siam Physics Congress SPC2012*, pp 213-215 (2012) เอกสารที่ 5 ในภาคผนวก

3.2 งานประชุมวิชาการ Siam Physics Congress (SPC) 2011 จัดโดยสมาคมฟิสิกส์แห่งประเทศไทย 23-26 มี.ค. 2554 จ.พัทยา ประเทศไทย

3.3 งาน ASEAN Workshop on Photoemission Electron Spectroscopy and Microscopy (AWPESM 2011) จัดโดยสถาบันวิจัยแสงซินโครตรอน 9-10 มิ.ย. 2554 จ. นครราชสีมา ประเทศไทย

3.4 งานสัมมนา The 3rd Annual UK-NL Condensed Matter Meeting เพื่อบรรยายในเรื่อง Creation and control of a two-dimensional electronliquid at the bare SrTiO3 surface วันที่ 2 ก.ย. 2553 จัดโดย University of Cambridge, Cambridge ในสหราชอาณาจักร

3.5 งานสัมมนา ALS/CXRO Seminars เพื่อบรรยายในเรื่อง Two-dimensional electron liquids at bare transition-metal oxide surfaces วันที่ 18 พ.ค. 2554 จัดโดย Advanced Light Source, Lawrence National Berkeley Lab. ในสหรัฐอเมริกา

ภาคผนวก

เอกสารที่ 1

W. Meevasana, P. D. C. King, R. H. He, S-K. Mo, M. Hashimoto, A. Tamai, P. Songsiriritthigul, F. Baumberger and Z-X. Shen, “Creation and control of a two-dimensional electron liquid at the bare $SrTiO_3$ surface”, *Nature Materials* 10, 114-118 (2011)

LETTERS
PUBLISHED ONLINE: 16 JANUARY 2011 | DOI: 10.1038/NMAT2943
nature materials

Creation and control of a two-dimensional electron liquid at the bare $SrTiO_3$ surface

W. Meevasana[1,2,3,4,5†], P. D. C. King[3†], R. H. He[1,2,6], S-K. Mo[1,6], M. Hashimoto[1,6], A. Tamai[3], P. Songsiriritthigul[4,5], F. Baumberger[3] and Z-X. Shen[1,2*]

Many-body interactions in transition-metal oxides give rise to a wide range of functional properties, such as high-temperature superconductivity[1], colossal magnetoresistance[2] or multiferroicity[3]. The seminal recent discovery of a two-dimensional electron gas (2DEG) at the interface of the insulating oxides $LaAlO_3$ and $SrTiO_3$ (ref. 4) represents an important milestone towards exploiting such properties in all-oxide devices[5]. This conducting interface shows a number of appealing properties, including a high electron mobility[4,6], superconductivity[7] and large magnetoresistance[8], and can be patterned on the few-nanometre length scale. However, the microscopic origin of the interface 2DEG is poorly understood. Here, we show that a similar 2DEG, with an electron density as large as 8×10^{13} cm^{-2}, can be formed at the bare $SrTiO_3$ surface. Furthermore, we find that the 2DEG density can be controlled through exposure of the surface to intense ultraviolet light. Subsequent angle-resolved photoemission spectroscopy measurements reveal an unusual coexistence of a light quasiparticle mass and signatures of strong many-body interactions.

It has been known for decades that strong electron correlations in oxide materials give rise to a rich variety of electronic phases, which are highly susceptible to small changes of control parameters. Although this situation is ideal for applications, the potential of all-oxide electronic devices had been questioned until very recently. Indeed, it was thought that the chemical complexity of most oxides would yield devices much inferior to those based on conventional semiconductors[5]. A paradigm shift came when unprecedented control of the complex $LaAlO_3/SrTiO_3$ interface was demonstrated[4], leading to the formation of a high-mobility electron gas[6]. The carrier density and sheet conductivity of the interface 2DEG react sensitively to gate fields and it was successfully patterned on the nanoscale[9], which is central to the development of oxide electronics[10]. However, a full understanding of the origin of this 2DEG remains elusive. The two main contenders are oxygen vacancies at the interface[11,12], and an electronic reconstruction to avoid a polar catastrophe[4,13]. Distinguishing between these mechanisms is an essential step in the development of a new generation of all-oxide devices.

Here, we show that a similar 2DEG can be created at the bare, unreconstructed $SrTiO_3$ surface. Furthermore, we demonstrate control of its carrier density through exposure to intense ultraviolet radiation. Figure 1 shows angle-resolved photoemission spectroscopy (ARPES) data from the cleaved (001) surface of

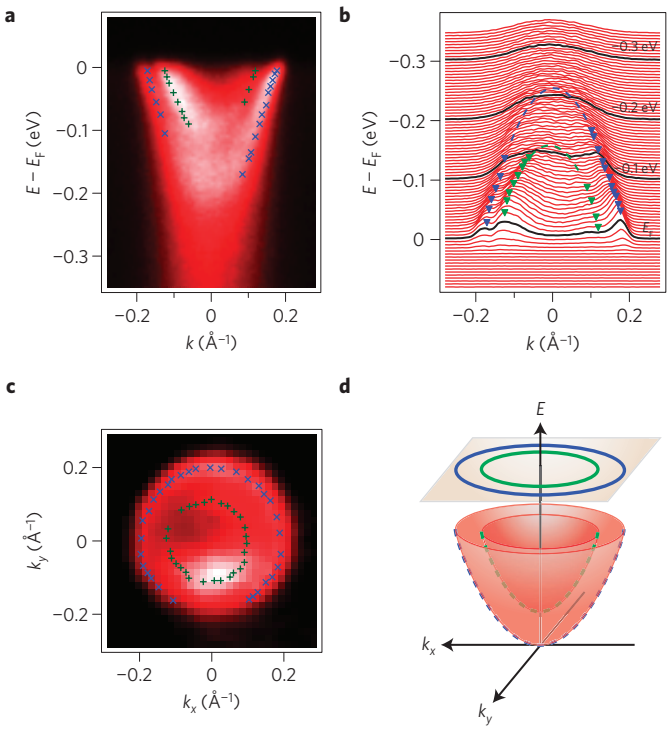

Figure 1 | Observation of a surface 2DEG on $SrTiO_3$ after exposure of the cleaved (100) surface to synchrotron (ultraviolet) light. a,**b**, ARPES data of $La_xSr_{1-x}TiO_3$ ($x = 0.001$) at $T = 20$ K (**a**), with corresponding momentum distribution curves (**b**). The sample has been irradiated with ≈480 J cm^{-2} ultraviolet light of 55 eV with an intensity of ~0.34 W cm^{-2}. The ARPES data are taken in the second Brillouin zone using the same photon energy. The dashed lines in **b** are parabolic fits to the data points (symbols) extracted from the ARPES data; the green and blue curves have effective masses of ~0.6 and $0.5m_e$, respectively. **c**, Fermi surface map, taken on a different sample following the same preparation. Two concentric circular Fermi surface sheets (symbols) are visible. **d**, The schematic Fermi surface and band dispersions obtained from the measured electronic structure.

0.1% La-doped $SrTiO_3$(001) following exposure to ultraviolet synchrotron light. At least two electron-like band dispersions can be observed from the ARPES data (Fig. 1a,b). The shallower band, with Fermi wave number $k_F = 0.12$ Å^{-1}, and deeper band,

[1]Departments of Physics and Applied Physics, Stanford University, California 94305, USA, [2]Stanford Institute for Materials and Energy Sciences, SLAC National Accelerator Laboratory, 2575 Sand Hill Road, Menlo Park, California 94025, USA, [3]School of Physics and Astronomy, University of St. Andrews, North Haugh, St. Andrews, KY16 9SS, UK, [4]School of Physics, Suranaree University of Technology and Synchrotron Light Research Institute, Nakhon Ratchasima, 30000, Thailand, [5]Thailand Center of Excellence in Physics, CHE, Bangkok, 10400, Thailand, [6]Advanced Light Source, Lawrence Berkeley National Lab, Berkeley, California 94720, USA. †These authors contributed equally to this work. *e-mail: zxshen@stanford.edu.

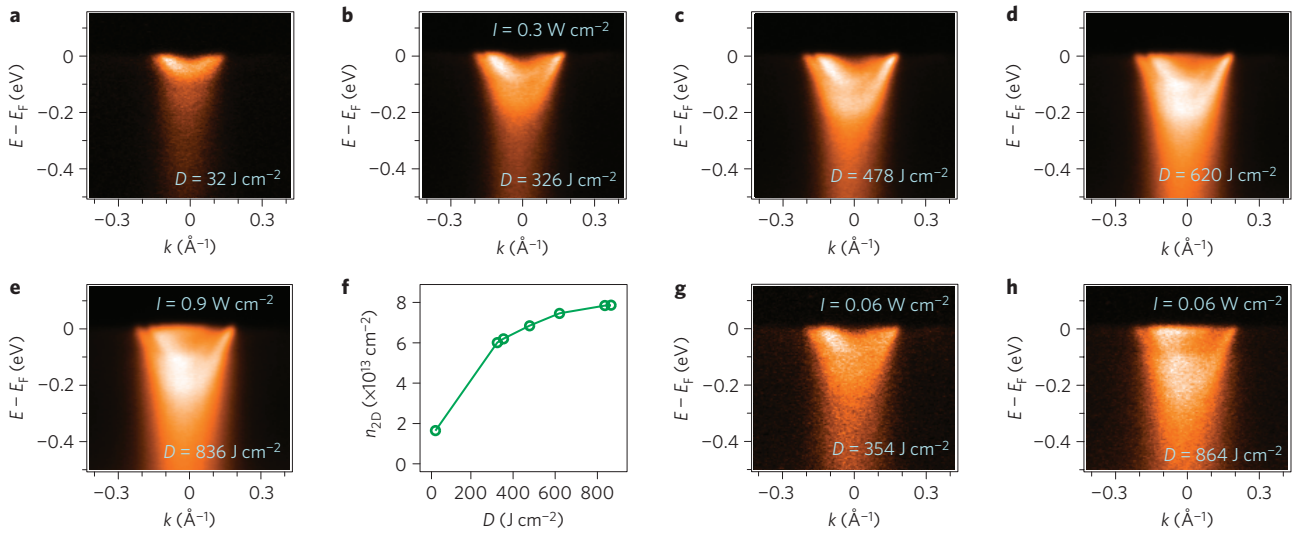

Figure 2 | Variation of 2DEG charge density with exposure to different ultraviolet irradiation doses. a–h, ARPES data for the specified irradiation doses (**a**–**e**,**g**,**h**), and the corresponding 2DEG charge densities as a function of irradiation dose, D (**f**). **g** and **h** show ARPES data measured immediately after **b** and **e**, respectively, but with a lower intensity of the probing photon beam.

with $k_F = 0.175$ Å^{-1}, have their band bottoms situated ~110 and 216 meV below the Fermi level, respectively. We have investigated the dimensionality of the induced electronic system by varying the photon energy, and thus probing the band dispersion along k_z (surface normal). Supplementary Fig. S2 shows that the states have negligible dispersion along k_z. This is the defining property of a two-dimensional (2D) electronic state whose wavefunction is confined along the z-direction to a layer of comparable thickness to the Fermi wavelength. In addition, these bands cannot be associated with the bulk electronic structure: the photon energy used to record the data shown in Fig. 1 corresponds to k_z of approximately $3.2\pi/a$ (ref. 14), close to the Brillouin zone boundary where no bulk bands exist in the vicinity of the Fermi energy, even for samples with more than an order of magnitude higher bulk carrier density than those measured here. Consequently, we attribute these states to a surface 2DEG.

To obtain the surface charge density, we extract the Luttinger area from the Fermi surface map shown in Fig. 1c. Two concentric Fermi surface sheets are observed, corresponding to the two dispersions in Fig. 1a. The intensity variation across the measured Fermi surface is due to pronounced matrix element effects. The charge density n_{2D} from each concentric sheet can then be estimated by $n_{2D} = k_F^2/2\pi$, allowing the total surface charge density to be determined as $7.1 \pm 2 \times 10^{13}$ cm^{-2}. This value falls within the range of the 2DEG densities observed at $LaAlO_3/SrTiO_3$ interfaces[7,11,12]. The effective masses extracted from parabolic fits to the two measured dispersions (Fig. 1a) yield surprisingly low values of $0.5–0.6m_e$, substantially lower than the bulk band masses. This will contribute to the high electron mobility[4].

Furthermore, as shown in Fig. 2, we find that the 2DEG density is not fixed to one particular value, but can be varied by exposure of the cleaved surface to different irradiation doses of ultraviolet light. We found no evidence of any 2DEG states from initial ARPES measurements of the freshly cleaved surface, indicating that the 2DEG forms only after exposure to ultraviolet light. Following exposure to 55 eV ultraviolet light for an irradiation dose of ~32 J cm^{-2} (Fig. 2a), we observe a single shallow band with $k_F \sim 0.1$ Å^{-1} and a band bottom ~60 meV below E_F. On increasing the irradiation dose, this band moves downwards, to higher binding energies, with a second band becoming visible between the first band and the Fermi level. The k_F positions and occupied bandwidth of these two bands continue to increase slowly with further increases in irradiation dose. The corresponding surface charge densities extracted from the measured bands are plotted in Fig. 2f, revealing a monotonic increase in 2DEG density with increasing irradiation dose. Therefore, the method used here provides a controllable means with which to modify the 2DEG density.

We note that Fig. 2g and h, which are measured immediately after Fig. 2b and e, respectively, but with a lower intensity of the probing beam ($I = 0.06$ W cm^{-2}), show identical band dispersions within experimental accuracy. Similar results have been obtained for spectra taken up to an hour after irradiation with an intense ultraviolet beam (not shown). This demonstrates that the 2DEG reported here is a ground-state property of the ultraviolet-irradiated $SrTiO_3$ surface. Hence, its origin must be fundamentally different from photocarrier doping effects, which have characteristic lifetimes of the excited states <1 ms at low temperature[15].

It is clear, therefore, that the irradiation by ultraviolet light mediates a change in the surface of the $SrTiO_3$, which consequently induces the 2DEG. Clear (1×1) low-energy electron diffraction patterns observed both before and after the ultraviolet exposure indicate that the surface does not reconstruct during this process (see Supplementary Fig. S1). Therefore, creation of a surface 2DEG brought about by a change in the intrinsic surface state distribution due to surface reconstruction can be ruled out. This indicates that extrinsic states, such as donor-like defects or adsorbates, induce the 2DEG. In particular, oxygen vacancies localized at the surface would be expected to lead to a surface electron accumulation, with charge neutrality requiring the creation of an electron 2DEG to screen the positive surface charge of such ionized defect centres. Experimental studies on $LaAlO_3/SrTiO_3$ interfaces[11,12] have shown that oxygen vacancies can be created during the sample preparation process under low oxygen pressures. Here, we suggest that exposure to intense ultraviolet light in ultrahigh vacuum causes oxygen desorption from the surface. Such a photon-induced chemical change was previously observed in photoluminescence spectra of $SrTiO_3$ following irradiation with 325 nm laser light[16], where a sub-bandgap luninescence peak, growing in magnitude with increasing irradiation, and stable for some time following the irradiation, was assigned to photo-induced oxygen vacancies. This is consistent with an increased in-gap defect state (ref. 17 and references therein) that we observe at ~1.3 eV below the Fermi level in angle-integrated photoemission spectra following the ultraviolet exposure (see Supplementary Information).

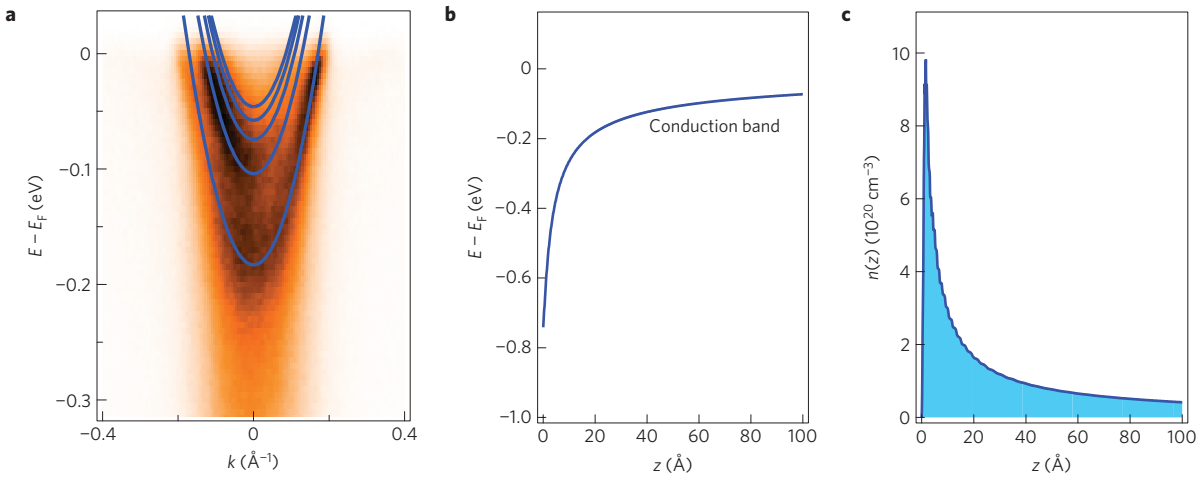

Figure 3 | Calculations of quantized 2DEG states within a band-bending model[20]. a,**b**, The calculations yield quantized 2DEG states (solid lines in **a**) inside the potential well caused by the downward bending of the conduction band minimum (solid line in **b**) relative to the Fermi level, when approaching the surface of the material. **c**, The corresponding 3D charge density variation as a function of depth, *z*. We note that in the calculation, there are three additional shallow states that are not clearly observed in the data. It is possible that these states exist in the data but are suppressed owing to a combination of matrix element effects and broadening due to finite k_z dispersion of the shallow states. These considerations are supported by the observations from InAs (Fig. 4b), as well as other semiconductors[24,28], where shallow states of a surface quantum well are more smeared out than the deeper ones.

We cannot exclude that this in-gap state could also arise from adsorbed impurities such as hydrogen, which could themselves provide the required donor-type surface states, as discussed in the Supplementary Information. However, irrespective of the exact microscopic identification of the defects causing the charge accumulation, the results presented above demonstrate that it is not necessary to have an interface with the polar surface of another material to obtain a 2DEG at the surface of $SrTiO_3$. Indeed, we find that extrinsic mechanisms are sufficient to induce a ground-state 2DEG of the same density. Apart from obvious advantages for their spectroscopic investigation, the methodology employed here to create such a 2DEG offers potential for the realization of new schemes in oxide electronics. Although existing approaches have the ability to pattern the spatial extent of the $LaAlO_3/SrTiO_3$ interface 2DEG (refs 9,18), our work opens the way to spatial control of its ground-state density by employing focused light. Furthermore, ultraviolet interference patterns could be used to allow much faster parallel nanoscale patterning of the 2DEG. This should not be specific to the surface of $SrTiO_3$, and could be employed for creation of surface 2DEGs across a range of oxide materials. The scheme should also be useful to write surface charge on $LaAlO_3$ by desorbing oxygen. For a thin layer of $LaAlO_3$ grown on $SrTiO_3$, charge localized at the surface of the $LaAlO_3$ is thought to provide the mechanism for writing of metallic lines at the $LaAlO_3/SrTiO_3$ interface using conducting atomic-force microscopy[19]. Writing of surface charge on the $LaAlO_3$ layer using ultraviolet interference patterns could therefore be an attractive route towards efficient processing of a high-mobility modulation-doped 2DEG, patterned at the nanoscale.

To further characterize the 2DEG created here, we adapt a model originally developed for conventional semiconductors[20]. The charge resulting from surface- (or indeed interface-) localized oxygen vacancies induces a spatial redistribution of bulk carriers in the vicinity of the surface/interface, correlated with a bending of the electronic bands relative to the Fermi level. If the potential well created by this band bending is sufficiently deep, it causes the conduction band states to become quantized into 2D sub-bands. We have carried out coupled Poisson–Schrödinger calculations[20] for such a band-bending scenario. Incorporating an electric-field dependence of the susceptibility[21] within our model, we find that the downward band bending in $SrTiO_3$ (Fig. 3b) is indeed very rapid. This leads to a narrow 2DEG (Fig. 3c) in a 3D crystal due only to the strength of the internal electric field. Its lowest sub-band is localized within ≈4 unit cells from the surface and is followed by a series of higher sub-bands with wavefunctions that progressively extend deeper into the bulk (see Supplementary Fig. S4). As shown in Fig. 3a, these sub-bands effectively reproduce the two main dispersions observed in the ARPES data, confirming that the states observed here can broadly be described as the quantum-well states of a surface 2DEG resulting from a downward band bending. The additional weakly bound states found in the calculations at lower binding energies are not resolved experimentally. This is possibly due to low matrix elements for shallow quantum-well states, which generally have small amplitudes of the wavefunction in the near-surface region probed by ARPES, as shown in Supplementary Fig. S4. Furthermore, as the wavefunctions of these shallow states expand over a much larger depth than the more localized deeper states, the shallow states might start dispersing in k_z, causing them to become smeared out in the ARPES measurements, possibly beyond our detection limit.

Our model does not take intra-unit-cell potential variations into account, thought to be important for the relatively local Ti 3*d* states. Nonetheless, it is in good qualitative agreement with density-functional theory calculations for the $LaAlO_3/SrTiO_3$ interface[22], which report a similar reconstruction of the electronic structure in the 2DEG into a ladder of sub-bands. The lowest of these was identified as an in-plane Ti d_{xy} state largely localized on the interfacial TiO_2 layer, whereas the charge density from a series of higher-lying d_{xy} states appeared spread out over several layers in the calculation. In addition, these authors found d_{yz}- and d_{xz}-derived states with strongly elliptical Fermi surfaces and high effective masses for transport along x and y, respectively. In the present case, we observe only two concentric isotropic Fermi surfaces of light carriers, which we attribute to the lowest members of a ladder of d_{xy} states. However, we cannot rule out the additional presence of heavy $d_{xz/yz}$ bands in the surface 2DEG, because their intensity would be suppressed relative to d_{xy} states in the experimental geometry and polarization employed here. In addition, the Fermi level in our experiment lies closer to the lowest sub-band minimum than in density functional theory calculations[22] for the $LaAlO_3/SrTiO_3$ interface, and so the $d_{xz/yz}$ states, if present,

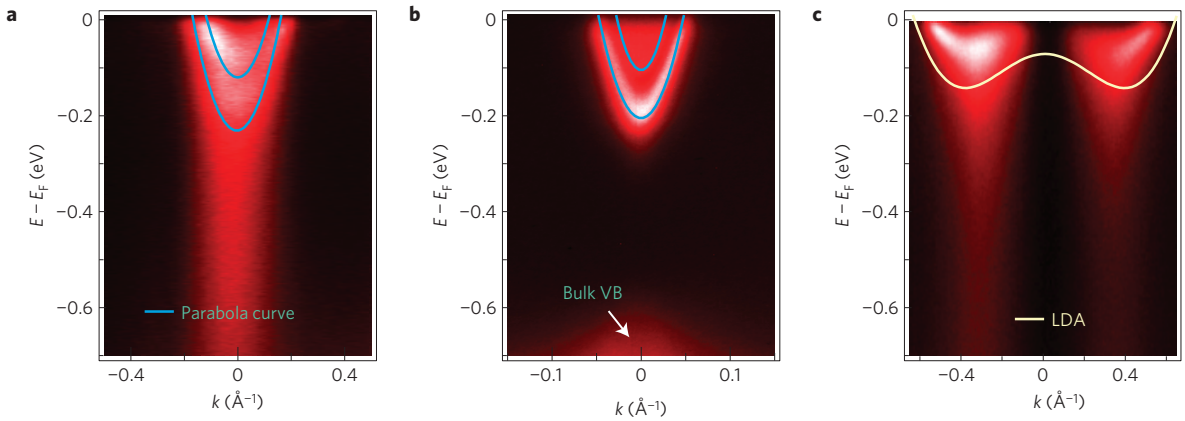

Figure 4 | Comparison of ARPES data from $SrTiO_3$, InAs and $Bi_2Sr_2CuO_6$ samples. a,**b**, 2DEG states at the surface of $SrTiO_3$ (**a**) and InAs (**b**). **c**, ARPES data from the single-layer cuprate $Bi_2Sr_2CuO_6$ (Bi2201) along $(\pi, 0)$ to $(0, \pi)$. The lines in **a** and **b** are parabolic dispersion relations, to guide the eye, and the result of a local density approximation band-structure calculation in **c**.

should be quite shallow and hence extend deep in the bulk, which would reduce their intensity in ARPES.

Although most conventional semiconductors exhibit a depletion of charge carriers at the surface, a small number have themselves been observed to support a surface 2DEG, concomitant with a downward band bending (ref. 23 and references therein). Comparing the 2DEG states from one such example, InAs (ref. 24) shown in Fig. 4b, with those of $SrTiO_3$ observed here (Fig. 4a), reveals a qualitative similarity between the two materials. This further confirms the validity of the above model. However, some important differences are also apparent. In particular, there is pronounced spectral weight in $SrTiO_3$ at binding energies much higher than the band bottom. This effect is absent for the semiconductor case, but can be seen in ARPES measurements of other strongly correlated compounds such as the cuprate high-temperature superconductor $Bi_2Sr_2CuO_6$ (Fig. 4c; ref. 25). The non-vanishing spectral weight in $SrTiO_3$ implies a finite electron self-energy at high binding energies, giving direct evidence of enhanced many-body interactions inherent to the 2DEG states of $SrTiO_3$. Hence, the 2DEG here is best described as an electron liquid rather than an electron gas[26]. Besides this spectral weight below the band bottom, we also note that the $SrTiO_3$ data show weak dispersion anomalies (kinks) at a binding energy around 20–30 meV and, less clearly, around 70–80 meV below the Fermi level, which we assign to electron–phonon interactions with a weaker coupling strength than observed in the bulk[14].

In systems where electronic correlations play an important role, the quasiparticles are normally found to be heavy. Intriguingly, however, the strong electron correlations we observe here do not lead to a substantial mass enhancement within the 2DEG. In fact, the effective mass of $0.5–0.6m_e$ extracted from the data is lower than the lightest bulk band mass of $\sim m_e$ estimated from ref. 14. Almost certainly, this will apply to the $LaAlO_3/SrTiO_3$ interface 2DEG too, which helps to explain the high electron mobilities achieved in this system. Although a direct spectroscopic measurement of the electronic band dispersion within the 2DEG, as carried out here, has not yet been achieved in the interface systems, this conclusion is supported by very recent measurements of the penetration field in front-gated $LaAlO_3/SrTiO_3$ heterostructures, where a 2DEG band mass significantly below any of the bulk masses was inferred[27]. We speculate that this unusual behaviour might be due to an interaction-induced shrinkage of the fundamental bandgap approaching the surface of $SrTiO_3$ (ref. 24). This would effectively increase the depth of the potential well and hence result in steeper quantized bands/lighter band masses. If this picture is true, the surface of $SrTiO_3$, or indeed its interface with $LaAlO_3$, is a rare example where many-body interactions have the counter-intuitive effect of increasing the mobility. A full understanding of this will require further theoretical and experimental studies. Spectroscopic investigations of surface 2DEGs, of the form reported here, will probably prove essential to elucidate the fundamental electronic structure and underlying role of many-body interactions in oxide 2DEGs, and so will play a major role in the development of all-oxide electronics.

Received 15 June 2010; accepted 10 December 2010; published online 16 January 2011

References

1. Bednorz, J. G. & Muller, K. A. Perovskite-type oxides: The new approach to high-Tc superconductivity. *Rev. Mod. Phys.* **60,** 585–600 (1988).
2. Von Helmolt, R. *et al.* Giant negative magnetoresistance in perovskitelike $La_{2/3}Ba_{1/3}MnO_x$ ferromagnetic films. *Phys. Rev. Lett.* **71,** 2331–2333 (1993).
3. Kimura, T. *et al.* Magnetic control of ferroelectric polarization. *Nature* **426,** 55–58 (2003).
4. Ohtomo, A. & Hwang, H. . A high-mobility electron gas at the $LaAlO_3/SrTiO_3$ heterointerface. *Nature* **427,** 423–426 (2004).
5. Takagi, H. & Hwang, H. Y. An emergent change of phase for electronics. *Science* **327,** 1601–1602 (2010).
6. Thiel, S. *et al.* Tunable quasi-two-dimensional electron gases in oxide heterostructures. *Science* **313,** 1942–1945 (2006).
7. Reyren, N. *et al.* Superconducting interfaces between insulating oxides. *Science* **317,** 1196–1199 (2007).
8. Brinkman, A. *et al.* Magnetic effects at the interface between non-magnetic oxides. *Nature Mater.* **6,** 493–496 (2007).
9. Cen, C. *et al.* Nanoscale control of an interfacial metal–insulator transition at room temperature. *Nature Mater.* **7,** 298–302 (2008).
10. Mannhart, J. & Scholm, D. G. Oxide interfaces—an opportunity for electronics. *Science* **327,** 1607–1611 (2010).
11. Siemons, W. *et al.* Origin of charge density at $LaAlO_3$ on $SrTiO_3$ heterointerfaces: Possibility of intrinsic doping. *Phys. Rev. Lett.* **98,** 196802 (2007).
12. Kalabukhov, A. *et al.* Effect of oxygen vacancies in the $SrTiO_3$ substrate on the electrical properties of the $LaAlO_3/SrTiO_3$ interface. *Phys. Rev. B* **75,** 121404(R) (2007).
13. Nakagawa, N., Hwang, H. Y. & Muller, D. A. Why some interfaces cannot be sharp. *Nature Mater.* **5,** 204–209 (2006).
14. Meevasana, W. *et al.* Strong energy–momentum dispersion of phonon-dressed carriers in the lightly doped band insulator $SrTiO_3$. *New. J. Phys.* **12,** 023004 (2010).
15. Kozuka, Y. *et al.* Optically tuned dimensionality crossover in photocarrier-doped $SrTiO_3$: Onset of weak localization. *Phys. Rev. B* **76,** 085129 (2007).
16. Mochizuki, S. *et al.* Photoluminescence and reversible photo-induced spectral change of $SrTiO_3$. *J. Phys. Condens. Matter* **17,** 923–948 (2005).
17. Aiura, Y. *et al.* Photoemission study of the metallic state of lightly electron-doped $SrTiO_3$. *Surf. Sci.* **515,** 61–74 (2002).
18. Caviglia, A. D. *et al.* Electric field control of the $LaAlO_3/SrTiO_3$ interface ground state. *Nature* **456,** 624–627 (2008).

19. Xie, Y. *et al.* Charge writing at the $LaAlO_3/SrTiO_3$ surface. *Nano Lett.* **10,** 2588–2591 (2010).
20. King, P. D. C., Veal, T. D. & McConville, C. F. Non-parabolic coupled Poisson–Schrodinger solutions for quantized electron accumulation layers: Band bending, charge profile, and subbands at InN surfaces. *Phys. Rev. B* **77,** 125305 (2008).
21. Copie, O. *et al.* Towards two-dimensional metallic behavior at $LaAlO_3/SrTiO_3$ interfaces. *Phys. Rev. Lett.* **102,** 216804 (2009).
22. Popović, Z. S., Satpathy, S. & Martin, R. M. Origin of the two-dimensional electron gas carrier density at the $LaAlO_3$ or $SrTiO_3$ interface. *Phys. Rev. Lett.* **101,** 256801 (2008).
23. King, P. D. C. *et al.* Surface electron accumulation and the charge neutrality level in In_2O_3. *Phys. Rev. Lett.* **101,** 116808 (2008).
24. King, P. D. C. *et al.* Surface band gap narrowing in quantized electron accumulation layers. *Phys. Rev. Lett.* **104,** 256803 (2010).
25. Meevasana, W. *et al.* Hierarchy of multiple many-body interaction scales in high-temperature superconductors. *Phys. Rev. B* **75,** 174506 (2007).
26. Breitschaft, M. *et al.* Two-dimensional electron liquid state at $LaAlO_3$–$SrTiO_3$ interfaces. *Phys. Rev. B* **81,** 153414 (2010).
27. Li, L. *et al.* Large capacitance enhancement and negative compressibility of two-dimensional electronic systems at $LaAlO_3/SrTiO_3$ interfaces. Preprint at http://arxiv.org/pdf/1006.2847 (2010).
28. Colakerol, L. *et al.* Quantized electron accumulation states in indium nitride studied by angle-resolved photoemission spectroscopy. *Phys. Rev. Lett.* **97,** 237601 (2006).

Acknowledgements

We would like to thank H. Y. Hwang, H. Takagi, M. R. Beasley, J. L. M. van Mechelen, D. van der Marel, P. Reunchan and S. Limpijumnong for helpful discussions. W.M. would like to thank H. Nakajima and Y. Rattanachai for help with the resistivity measurement. The work at ALS and Stanford Institute for Materials and Energy Sciences is supported by DOE's Office of Basic Energy Sciences under Contracts No. DE-AC02-76SF00515 and DE-AC03-76SF00098. The work at St. Andrews is supported by the UK-EPSRC (EP/F006640/1) and the ERC (207901). W.M. acknowledges The Thailand Research Fund, Office of the Higher Education Commission and Suranaree University of Technology for financial support.

Author contributions

ARPES measurements were carried out by W.M., P.D.C.K., R.H.H., F.B. and A.T. W.M. and P.D.C.K. analysed the ARPES data. W.M., P.D.C.K. and F.B. wrote the paper with suggestions and comments by R.H.H., S-K.M. and Z-X.S. Calculations of quantized 2DEG states were done by P.D.C.K. S-K.M. and M.H. maintained the ARPES endstation. Resistivity measurements were carried out by W.M. and P.S. Z-X.S. and F.B. are responsible for project direction, planning and infrastructure.

Additional information

The authors declare no competing financial interests. Supplementary information accompanies this paper on www.nature.com/naturematerials. Reprints and permissions information is available online at http://npg.nature.com/reprintsandpermissions. Correspondence and requests for materials should be addressed to Z-X.S.

เอกสารที่ 2

P.D.C.King, J.A. Rosen, **W. Meevasana**, A. Tamai, E. Rozbicki, R. Comin, G. Levy, D. Fournier, Y. Yoshida, H. Eisaki, K.M. Shen, N.J.C. Ingle, A. Damascelli, F. Baumberger, “Structural origin of apparent Fermi surface pockets in angle-resolved photoemission of $Bi_2Sr_{2-x}La_xCuO_6$”, *Physical Review Letters* 106, 127005 (2011)

Structural Origin of Apparent Fermi Surface Pockets in Angle-Resolved Photoemission of $Bi_2Sr_{2-x}La_xCuO_{6+\delta}$

P. D. C. King,[1] J. A. Rosen,[2] W. Meevasana,[1,3] A. Tamai,[1] E. Rozbicki,[1] R. Comin,[2] G. Levy,[2] D. Fournier,[2] Y. Yoshida,[4] H. Eisaki,[4] K. M. Shen,[5] N. J. C. Ingle,[6] A. Damascelli,[2,7] and F. Baumberger[1,*]

[1]*School of Physics and Astronomy, University of St Andrews, North Haugh, St Andrews, KY16 9SS, United Kingdom*
[2]*Department of Physics and Astronomy, University of British Columbia, Vancouver, British Columbia V6T 1Z1, Canada*
[3]*School of Physics, Suranaree University of Technology, Nakhon Ratchasima, 30000 Thailand*
[4]*National Institute of Advanced Industrial Science and Technology, Tsukuba, Ibaraki 305-8568, Japan*
[5]*Laboratory of Atomic and Solid State Physics, Cornell University, Ithaca, New York 14853, USA*
[6]*AMPEL, University of British Columbia, Vancouver, British Columbia V6T 1Z1, Canada*
[7]*Quantum Matter Institute, University of British Columbia, Vancouver, British Columbia V6T 1Z4, Canada*

(Received 26 November 2010; published 24 March 2011)

We observe *apparent* hole pockets in the Fermi surfaces of single-layer Bi-based cuprate superconductors from angle-resolved photoemission. From detailed low-energy electron diffraction measurements and an analysis of the angle-resolved photoemission polarization dependence, we show that these pockets are not intrinsic but arise from multiple overlapping superstructure replicas of the main and shadow bands. We further demonstrate that the hole pockets reported recently from angle-resolved photoemission [Meng *et al.*, Nature (London) **462**, 335 (2009)] have a similar structural origin and are inconsistent with an intrinsic hole pocket associated with the electronic structure of a doped CuO_2 plane.

DOI: 10.1103/PhysRevLett.106.127005 PACS numbers: 74.72.Kf, 74.25.Jb, 74.72.Gh

The pseudogap is one of the defining properties of the hole-doped high-T_c superconductors [1]. Understanding its origin is widely regarded as a key to unravelling the mechanisms of the high transition temperature superconductivity in these materials. While above the pseudogap temperature T^* a large closed Fermi surface characteristic of ordinary metals is observed [2,3], at temperatures below T^* angle-resolved photoemission (ARPES) measurements have long revealed disconnected Fermi ''arcs,'' centered around the $(0, 0) \rightarrow (\pi, \pi)$ nodal direction [2,4–6]. Only recently, it has been claimed that distinct closed hole pockets can be observed by ARPES at particular compositions of the $Bi_2Sr_{2-x}La_xCuO_{6+\delta}$ (La-Bi2201) cuprate [7]. While this would be qualitatively consistent with the demonstration of quantum oscillations in underdoped cuprates, indicative of small closed pockets in a high field [8–13], it remains unclear how it can be reconciled with numerous earlier ARPES studies.

A key difficulty is the structural complexity of Bi-based cuprates. They possess an orthorhombic lattice distortion [14], which is likely the origin of the so-called shadow Fermi surface [15–18]. In addition, they are prone to single [14,18,19] or even multiple [20] superstructure modulations along the crystallographic b axis. These additional periodicities arise from a slight lattice mismatch between the BiO and CuO_2 planes and cause diffraction replica (DR) of electronic bands [21].

Here, we combine an extensive **k**-space survey of the Fermi-surface topology of La-substituted Bi2201 with a detailed structural analysis, in order to separate generic electronic effects from DR. We show that large superstructure periodicities of up to $14a_0$, coexisting with the already well-established periodicity of $\approx 4.2a_0$, are common. Such structural artifacts lead to imitations of closed Fermi-surface pockets in ARPES measurements. From their polarization dependence, we demonstrate that the front and back sides of the pockets derive from the main and shadow bands, respectively, and do not represent a single closed portion of Fermi surface intrinsic to the doped CuO_2 plane as claimed previously [7].

We investigated optimally (OP) and underdoped (UD) La-Bi2201 with $x = 0.5$ (OP30K), $x = 0.75$ (UD20K), and $x = 0.8$ (UD14.5K) and optimally doped $Bi_{1.7}Pb_{0.35}La_{0.4}Sr_{1.6}CuO_{6+\delta}$ [(Pb,La)-Bi2201, OP35K] samples. ARPES measurements on La-Bi2201 (Figs. 1 and 3) were performed in the pseudogap phase at $\sim$17.5 K and $\sim$33.5 K for UD14.5K and OP30K La-Bi2201, respectively, with linearly polarized He-Iα radiation ($h\nu = 21.22$ eV) and a SPECS Phoibos 225 hemispherical analyzer, while the data on (Pb,La)-Bi2201 (Fig. 2) were taken in the superconducting phase at 10 K with unpolarized light. The angular and energy resolutions for all measurements were set to 0.3° and better than 20 meV, respectively. All low-energy electron diffraction (LEED) patterns shown here were recorded at temperatures between $\sim T_c$ and $\sim 2T_c$ with an incident electron energy of 35 eV.

Figure 1(a) shows the Fermi surface of UD14.5K La-Bi2201 as measured by ARPES. Fermi arcs are visible centered around the nodal directions, although their intensity is suppressed along Γ-Y due to matrix element effects which we shall discuss later. Multiple copies of these arcs

can be observed, separated by ~ 0.28 Å^{-1} along the Γ-Y direction, consistent with DR corresponding to the established dominant superstructure periodicity of this material. In addition, weak features with opposite dispersion to the Fermi arcs appear to form several small closed pockets along the nodal direction (white arrows, p_1–p_4). These features cannot be observed in optimally doped La-Bi2201, shown in Fig. 1(b), consistent with the findings of Meng *et al.* [7].

In the following, we show that the closed pockets appear as a natural consequence of structural complications in La-Bi2201. Lines of periodic diffraction maxima, characteristic of superstructure modulation along the Γ-Y direction, are clearly discernible in the LEED pattern from OP30K La-Bi2201 [Fig. 1(d)]. From their spacing, the superstructure vector can be determined as $\mathbf{q}_i = (q_i, q_i)\frac{\pi}{a}$ with $q_1 = 0.235 \pm 0.015$, in agreement with the DR in the ARPES and with earlier diffraction studies [22]. Intriguingly, LEED from UD14.5K La-Bi2201 [Fig. 1(c)] shows not only a similar superstructure vector $q_1 = 0.245 \pm 0.015$ but exhibits yet further diffraction maxima revealing the coexistence of a second superstructure with $q_2 = 0.130 \pm 0.015$. In order to demonstrate how these superstructure periodicities lead to the impression of hole pockets in ARPES, we first fit a tight-binding model to the Fermi surface of the main band for each doping [solid black lines in Figs. 1(a) and 1(b)] and then translate this band by (π, π) to describe the shadow band resulting from the orthorhombic distortion. Finally, we add umklapp bands, that is, DR of the main and shadow bands, with the $\mathbf{q_i}$ vectors determined independently from LEED. Without any further adjustment this simple model reproduces the entire measured Fermi surfaces for the UD14.5K and the OP30K samples over an extensive k-space range. In particular, it describes all apparent hole pockets in the underdoped sample and the absence of these pockets in optimally doped La-Bi2201. For example, the pockets p_1 and p_3 in UD14.5K La-Bi2201 are created by the $\mathbf{q}_2$ DR of the shadow band crossing the main band, while another pocket (p_2) is formed by the $-\mathbf{q}_1$ DR of the main band overlapping the $-\mathbf{q}_2$ DR of the shadow band. All of these pockets are absent in OP30K La-Bi2201, which does not show the $\mathbf{q}_2$ periodicity in LEED. It is therefore evident that the seemingly closed portions of Fermi surface in underdoped La-Bi2201 are not intrinsic but appear from the overlapping of DR resulting from multiple superstructure periodicities.

We stress that the appearance of these pockets is not directly tied to the hole concentration, or the presence of a pseudogap, but rather to the particular structural modulations. Indeed, we also observe multiple superstructures, with vectors of $q_1 = 0.225 \pm 0.015$ and $q_2 = 0.072 \pm 0.015$, in optimally doped (Pb,La)-Bi2201 [Fig. 2(a)]. Although Pb doping tends to suppress superstructure-related features in ARPES from Bi-based cuprates, the measured Fermi surface [Fig. 2(b)] clearly shows the presence of umklapps resulting from these superstructure vectors and their combinations, consistent with a tight-binding model using the $\mathbf{q_i}$ vectors determined from LEED. Similar

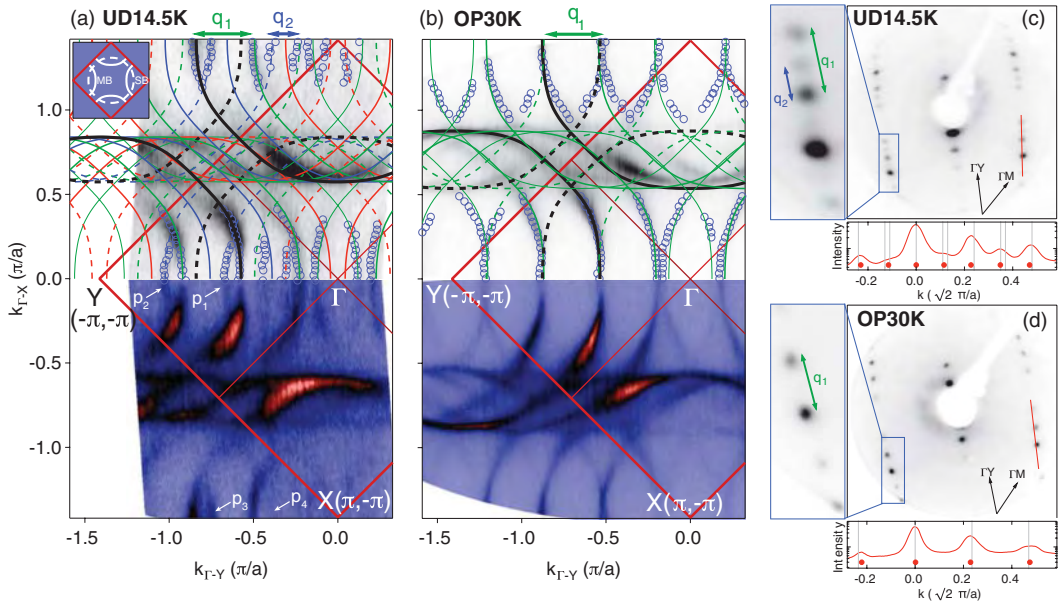

FIG. 1 (color online). ARPES Fermi surface of (a) UD14.5K and (b) OP30K La-Bi2201, measured with p polarization. Extracted contours (blue circles) and a tight-binding model of the main (solid line), shadow (dashed line), and $\pm\mathbf{q}_1$ or $\pm 2\mathbf{q}_1$ (green), $\pm\mathbf{q}_2$ (blue), and $\pm(\mathbf{q}_1 + \mathbf{q}_2)$ (red) umklapp bands are overlaid on the data. LEED from (c) UD14.5K and (d) OP30K La-Bi2201. A magnified view of the blue region and a line cut along the Γ-Y direction (red line) are shown to the left of and below each pattern, respectively. Extracted peak positions (red dots) and those expected for superstructure peaks at $\mathbf{k}_0 \pm m_1\mathbf{q}_1 \pm m_2\mathbf{q}_2$ (vertical gray lines) are in good agreement. The inset in (a) shows a simplified Fermi surface with only the main (MB) and shadow (SB) bands.

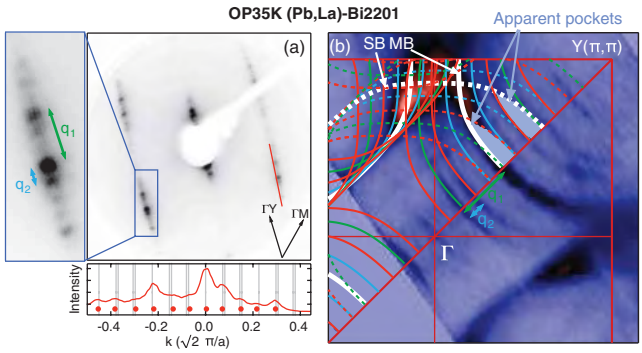

FIG. 2 (color online). (a) LEED pattern and (b) ARPES Fermi surface of OP35K (Pb,La)-Bi2201, showing the presence of two superstructure vectors, and the resulting apparent pockets in the Fermi surface. A tight-binding model, using superstructure vectors determined from the LEED analysis, is also shown in (b).

to the situation in underdoped La-Bi2201, the overlapping of several of these bands gives rise to features that appear as closed Fermi-surface pockets. However, as for UD14.5K La-Bi2201, this is entirely due to structural effects and should not be confused with either an intrinsic hole pocket or an incommensurate density-wave order.

The structural origin of the observed pockets can be further confirmed by polarization-dependent ARPES measurements, as shown in Fig. 3. The $x^2 - y^2$ symmetry of the hole in the Cu d shell is odd with respect to the Γ-Y direction. Consequently, for the experimental geometry employed here, with the incident light and detected electrons both within the horizontal plane, the main band can be observed when measuring with s-polarized light along the Γ-Y azimuth but is suppressed for p polarization. This is the reason why the intensity along the Fermi arc diminishes approaching the Γ-Y nodal line in Figs. 1(a) and 1(b). In contrast, the shadow band, which has the opposite parity of the main band [15], is visible in p polarization but not in s polarization. This switching of intensities is clearly seen for OP30K La-Bi2201 in Fig. 3(a) [23]. For measurements in the 2nd Brillouin zone, along the cut shown in Fig. 3(d), the polarization is no longer strictly s or p since the sample is tilted off-vertical by $\sim 30°$. Nevertheless, a strong relative intensity variation can still be observed between the main and shadow bands on switching from dominant p polarization (I_{MB}:I_{SB} smaller) to s polarization (I_{MB}:I_{SB} larger), as shown in Fig. 3(b). The equivalent dispersion measured in UD14.5K La-Bi2201 is shown in Fig. 3(c). With p polarization, two strong dispersions can be seen due to the main band and its $-\mathbf{q}_1$ DR, with two weaker neighboring bands which form the back side of the apparent Fermi-surface pockets (marked in the Fermi level momentum distribution curve by circles and crosses, respectively). This gives the appearance that the pocket on the Fermi surface is holelike, as claimed in Ref. [7]. However, on switching to s polarization, these "pocket-forming" bands are strongly suppressed relative to the main bands, as is the spectral intensity of the back side of all of the pocket features which can be seen in the ARPES Fermi surface [Fig. 3(d)]. This switching of intensities due to different parities of the front and back sides of the Fermi-surface pockets is difficult to reconcile with intrinsic pockets of a reconstructed Fermi surface and confirms that these features are derived from the shadow band.

Given this, one must revise the conclusions of Ref. [7] regarding intrinsic hole pockets. Meng *et al.* [7] considered only umklapp bands arising from a $q_1 \approx 0.24$ superstructure modulation and found that these DR could not explain their data. However, LEED from La-Bi2201 with very similar composition to the UD18K sample of Ref. [7] shows not only the $q_1 = 0.24$ superstructure but also a second superstructure with $q_2 = 0.12 \pm 0.015$ [see

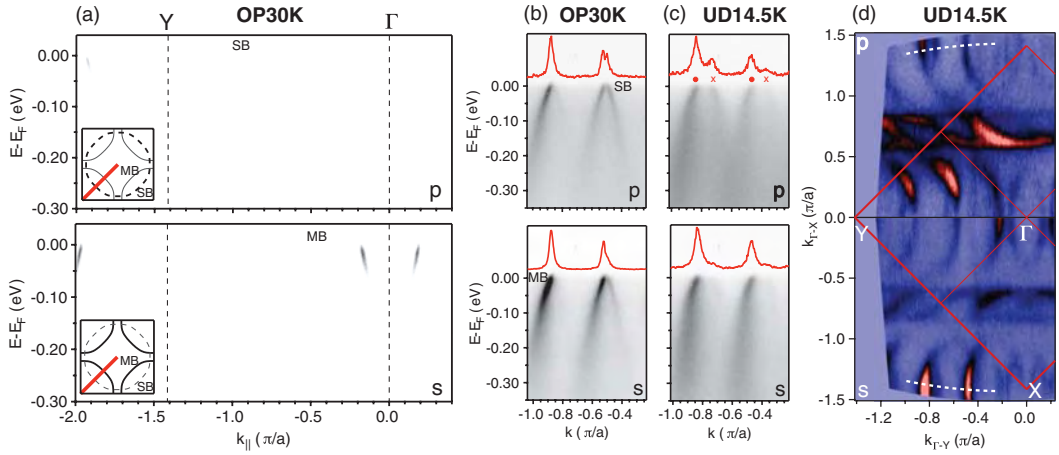

FIG. 3 (color online). Polarization dependence of ARPES. (a) Dispersion along Γ-Y of OP30K La-Bi2201. (b),(c) Dispersion close to the equivalent direction in the 2nd Brillouin zone [along dashed lines in (d)] of OP30K and UD14.5K La-Bi2201. (d) ARPES Fermi surface of UD14.5K La-Bi2201. All spectra were measured with p (top) and s (bottom) polarization.

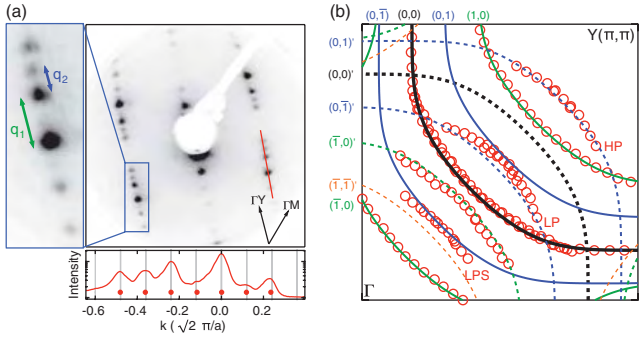

FIG. 4 (color online). (a) LEED of UD20K La-Bi2201. (b) Red circles reproduce the Fermi-surface contours of UD18K La-Bi2201 from Ref. [7]. A tight-binding Fermi surface including umklapp bands derived from our LEED analysis reproduces all features of the data from Meng *et al.* [7] including the apparent Fermi-surface pockets (labeled LP, HP, and LPS after Ref. [7]). The tight-binding bands are labeled by $(m_1, m_2)^{[']}$, where m_i is the order of the $(\mathbf{q}_1, \mathbf{q}_2)$ superstructure replica and a prime denotes the shadow band.

Fig. 4(a)]. In Fig. 4(b), we show that the measured pockets, and indeed all features of the Fermi-surface topology extracted in Ref. [7], are accurately described by a tight-binding model of only the conventional main and shadow bands, provided DR are included corresponding to both of these superstructure vectors. Together with the polarization-dependent ARPES presented above, this shows unambiguously that the observations of Meng *et al.* [7] have a trivial interpretation and cannot be taken as evidence for elusive Fermi pockets.

We also note that a structural origin of the pockets explains several puzzling observations of Ref. [7]. First, the main band (Fermi arc) was observed to be longer than the back side of the claimed pocket [as is also evident here in Figs. 1(a) and 2(b)]. The lower intensity of the shadow band and its DRs, which appear to ''close'' the pockets, compared to the main band naturally accounts for this seemingly contradictory coexistence of Fermi arcs and hole pockets. Second, the spectral weight of the back side of the pockets in Ref. [7] appears largest close to the nodal line. This is in contrast to theoretical expectations for an intrinsic pocket [24,25] but consistent with a superstructure replica of the shadow band. Third, multiple hole pockets were observed in Ref. [7], attributed to a $q = 0.24$ superstructure replica of a single intrinsic pocket. However, the front- to back-side spectral weight ratio differs for these pockets. Again this suggests that the two sides of the pockets derive from different bands, namely, the main and shadow band, whose umklapps display complex intensity variation due to matrix element effects. In addition, the superstructure vectors depend sensitively on doping as shown from the LEED analysis presented here, which provides a simple explanation for the unusual doping dependence of the hole pockets reported by Meng *et al.* [7].

We note that our findings do not exclude the presence of intrinsic Fermi-surface pockets in cuprates, where the back side of the pocket has negligible spectral weight in ARPES measurements [26]. However, we remark that, to date, clearly discernible hole pockets have been reported only from ARPES measurements in Bi-based and La-based cuprate systems [7,27], which are both subject to structural distortions. No such observation has been made in compounds free of such distortions, for example, CCOC [5] and YBCO [28].

We acknowledge financial support from the Scottish Funding Council, the United Kingdom EPSRC (Grant No. EP/F006640), the ERC [St Andrews], the Killam program, the Sloan Foundation, the CRC program, NSERC, CFI, CIFAR Quantum Materials, BCSI [UBC], TRF-OHEC [Suranaree], and NSF Grant No. DMR-0847345 [Cornell].

*fb40@st-andrews.ac.uk

[1] T. Timusk and B. Statt, Rep. Prog. Phys. **62**, 61 (1999).
[2] A. Kanigel *et al.*, Nature Phys. **2**, 447 (2006).
[3] M. Hashimoto *et al.*, Nature Phys. **6**, 414 (2010).
[4] M. R. Norman *et al.*, Nature (London) **392**, 157 (1998).
[5] K. M. Shen *et al.*, Science **307**, 901 (2005).
[6] T. Valla *et al.*, Science **314**, 1914 (2006).
[7] J. Meng *et al.*, Nature (London) **462**, 335 (2009).
[8] N. Doiron-Leyraud *et al.*, Nature (London) **447**, 565 (2007).
[9] E. A. Yelland *et al.*, Phys. Rev. Lett. **100**, 047003 (2008).
[10] A. F. Bangura *et al.*, Phys. Rev. Lett. **100**, 047004 (2008).
[11] D. LeBoeuf *et al.*, Nature (London) **450**, 533 (2007).
[12] S. E. Sebastian *et al.*, Nature (London) **454**, 200 (2008).
[13] M. R. Norman, Physics **3**, 86 (2010).
[14] M. A. Subramanian *et al.*, Science **239**, 1015 (1988).
[15] A. Mans *et al.*, Phys. Rev. Lett. **96**, 107007 (2006).
[16] K. Nakayama *et al.*, Phys. Rev. B **74**, 054505 (2006).
[17] P. Aebi *et al.*, Phys. Rev. Lett. **72**, 2757 (1994).
[18] N. L. Saini *et al.*, Phys. Rev. Lett. **79**, 3467 (1997).
[19] R. L. Withers *et al.*, J. Phys. C **21**, L417 (1988).
[20] W. L. Yang *et al.*, Physica (Amsterdam) **308C**, 294 (1998).
[21] Throughout, we distinguish the (π, π) umklapp of the main band, giving rise to the shadow band, from the superstructure diffraction replica to be consistent with conventional terminology.
[22] L. Dudy *et al.*, J. Supercond. Novel Magnetism **22**, 51 (2009).
[23] The lack of complete suppression of the forbidden transitions is due to the finite degree of polarization ($\sim 80\%$) of the incident light in the experimental setup used here.
[24] S. Chakravarty, C. Nayak, and S. Tewari, Phys. Rev. B **68**, 100504 (2003).
[25] K.-Y. Yang, T. M. Rice, and F.-C. Zhang, Phys. Rev. B **73**, 174501 (2006).
[26] H.-B. Yang *et al.*, Nature (London) **456**, 77 (2008).
[27] J. Chang *et al.*, New J. Phys. **10**, 103016 (2008).
[28] M. A. Hossain *et al.*, Nature Phys. **4**, 527 (2008).

เอกสารที่ 3

J. Osaklunga, C.Euaruksakul, **W.Meevasana***, P.Songsiriritthigul, “Spatial variation of the number of graphene layers formed on the scratched 6H–SiC(0001) surface”, *Applied Surface Science* 258, 4672-4677 (2012)

Applied Surface Science 258 (2012) 4672–4677

Contents lists available at SciVerse ScienceDirect

Applied Surface Science

journal homepage: www.elsevier.com/locate/apsusc

Spatial variation of the number of graphene layers formed on the scratched 6H–SiC(0 0 0 1) surface

J. Osaklung[a,b], C. Euaruksakul[c,d], W. Meevasana[a,c,d,*], P. Songsiriritthigul[a,c,d]

[a] School of Physics, Suranaree University of Technology, Nakhon Ratchasima 30000, Thailand
[b] Department of Physics, Faculty of Science, Kasetsart University, Bangkok 10900, Thailand
[c] Synchrotron Light Research Institute, Nakhon Ratchasima 30000, Thailand
[d] Thailand Center of Excellence in Physics, CHE, Bangkok 10400, Thailand

ARTICLE INFO

Article history:
Received 15 September 2011
Received in revised form 10 January 2012
Accepted 10 January 2012
Available online 18 January 2012

Keywords:
Epitaxial graphene
SiC
Low-energy electron microscopy
Substrate scratch

ABSTRACT

The unique properties of graphene can vary greatly depending on the number of graphene layers; therefore, spatial control of graphene thickness is desired to fully exploit these properties in promising new devices. Using low energy electron microscopy (LEEM), we investigate how scratches on the surface of 6H–SiC(0 0 0 1) affect the epitaxial growth of graphene. Oscillations in the LEEM-image intensity as a function of electron energy (I–V LEEM analysis) show that the number of graphene layers clearly differs between regions of scratched and smooth substrate. The extent of the thicker graphene layers formed above scratches is found to be significantly larger than the width of the scratch itself. This finding can be implemented as an additional technique for spatially modulating graphene thickness.

1. Introduction

After Geim and Novoselov discovered graphene, a single atomic layer of graphite, in 2004 by exfoliating highly oriented pyrolytic graphite[1], many unique electronic properties of graphene have been reported, including extremely-high mobility [2], ambipolar behavior [2], the room-temperature quantum hall effect [3], and plasmarons [4]. These unique properties and the abundance of carbon materials promise carbon-based electronic devices with superior performance and novel functionalities over current semiconductor devices.

As the properties of graphene are largely dependent on the number of layers, (e.g. bandgap opening [5,6] and plasmaron coupling [4]), many recent studies have focused on methods for growing a precise number of graphene layers. There are various methods for creating graphene such as the drawing technique (mechanical exfoliation of graphite crystals) [7], epitaxial growth on semiconductor [2] and metal [8,9] substrates, and chemical vapor deposition (CVD) [10,11]. Epitaxial graphene prepared on silicon-carbide (SiC) is a method which produces a particularly high quality graphene. By using this method, many interesting results such as the relativistic electronic structure (so-called "Dirac cone") [12], bandgap opening [13], and anomalous quantum Hall effect [14,15] have been reported. However, to exploit these properties for industrial purposes, graphene growth over a decently large area and the ability to pattern the graphene with different numbers of layers is still under development. So far, the in-plane size of uniform graphene by using this method is limited to around 3 μm × 50 μm as reported by Emtsev et al. [16], and 50 μm^2 as reported by Virojanadara et al. [17]. One of the factors limiting growth beyond this size could be the roughness of or scratches on SiC surfaces [18]. Note that the graphene grown using the CVD technique [10] can actually be much larger in the order of centimeters; however, the quality of this graphene can be inferior to epitaxial graphene as the reported carrier mobility of CVD-grown graphene appears to be much lower than that of epitaxial graphene (e.g. approximately 7 times lower comparing Ref. [10] and Ref. [19]).

To better understand the formation and shape of epitaxially grown graphene, in this paper, we look into the effect that substrate scratches (~0.2 μm in width) have on the spatial variation of graphene layers formed on a 6H–SiC(0 0 0 1) surface. By using low-energy electron microscopy (LEEM), we extract the number of graphene layers over selected surface areas using a I–V (Intensity–Voltage) analysis of the LEEM images [20]. The number of layers is observed to be higher near the scratched areas and importantly the thicker graphene layers can have a width as large as 2.5 times of the scratch width itself (see Fig. 4).

* Corresponding author at: School of Physics, Suranaree University of Technology, Nakhon Ratchasima 30000, Thailand. Tel.: +66 44 224 291; fax: +66 44 224 651.
E-mail address: worawat@g.sut.ac.th (W. Meevasana).

0169-4332/$ – see front matter © 2012 Elsevier B.V. All rights reserved.
doi:10.1016/j.apsusc.2012.01.059

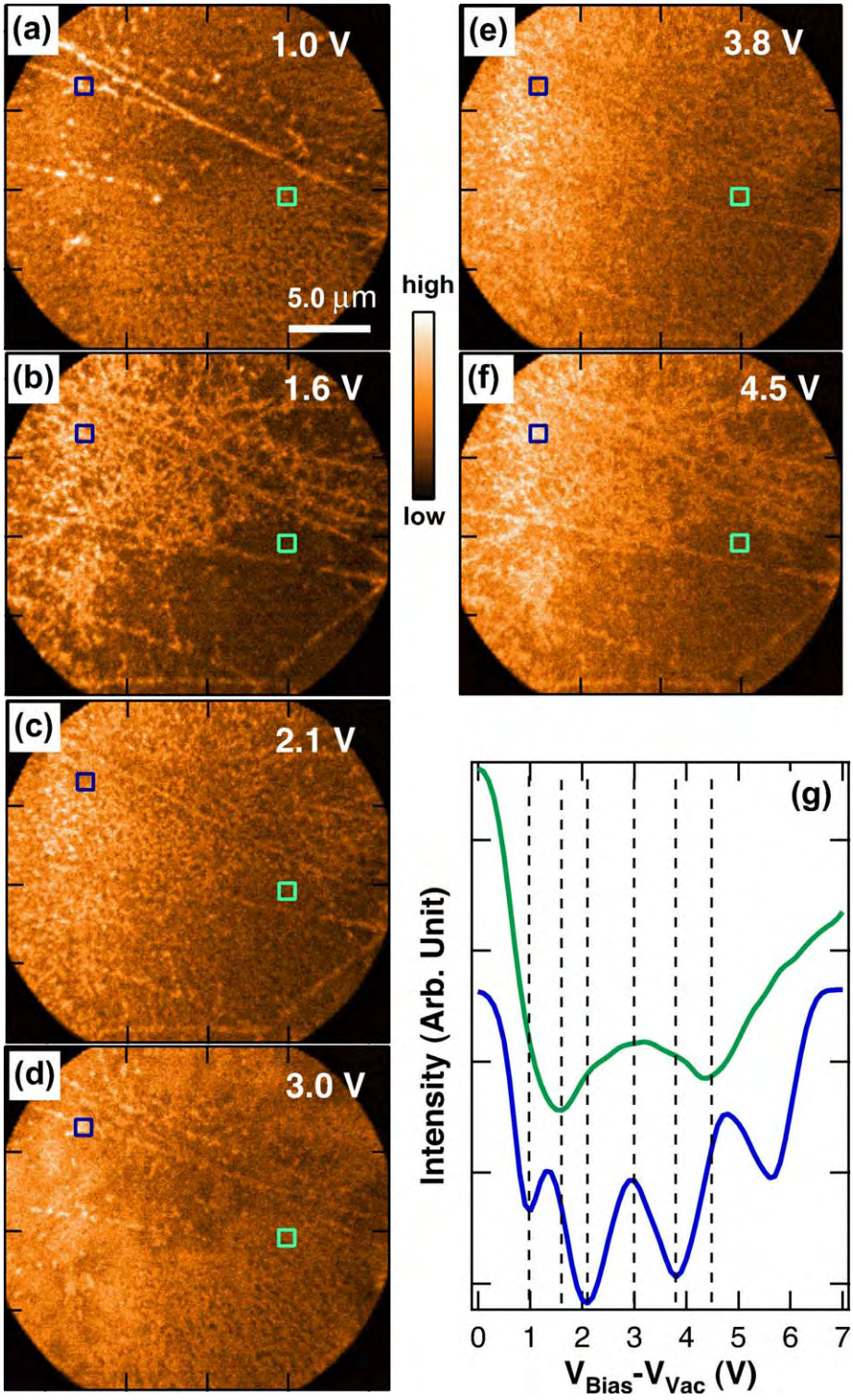

Fig. 1. LEEM images of the graphene grown on the scratched SiC substrate at various adjusted bias voltages ($V_{Bias} - V_{Vac}$) of the incident electron: (a) 1.0, (b) 1.6, (c) 2.1, (d) 3.0, (e) 3.8 and (f) 4.5 V. (g) shows the plots of intensity at the two selected spots (blue and green squares in (a)–(f)) as a function of bias voltage (I–V LEEM plot); note that the two plots are offset by the two intensities at $V_{Bias} - V_{Vac} = 0$ V. (For interpretation of the references to color in this figure legend, the reader is referred to the web version of the article.)

2. Materials and methods

In this study, the epitaxial graphene layers were grown on a 6H–SiC(0 0 0 1) substrate by thermal decomposition in an ultra-high vacuum environment. The *n*-type doped 6H–SiC(0 0 0 1) (MTI Corporation) is one side polished. The dimension of the substrate is 5 mm × 5 mm × 0.3 mm with the axis of orientation ⟨0 0 0 1⟩. The surface topography of the substrate was examined by atomic force microscopy (AFM) in AC mode. An AFM image was taken after chemical cleaning (shown in Fig. 3a). Another one was then taken after a short annealing process (not shown) but it does not show a significant difference. Both were taken before the

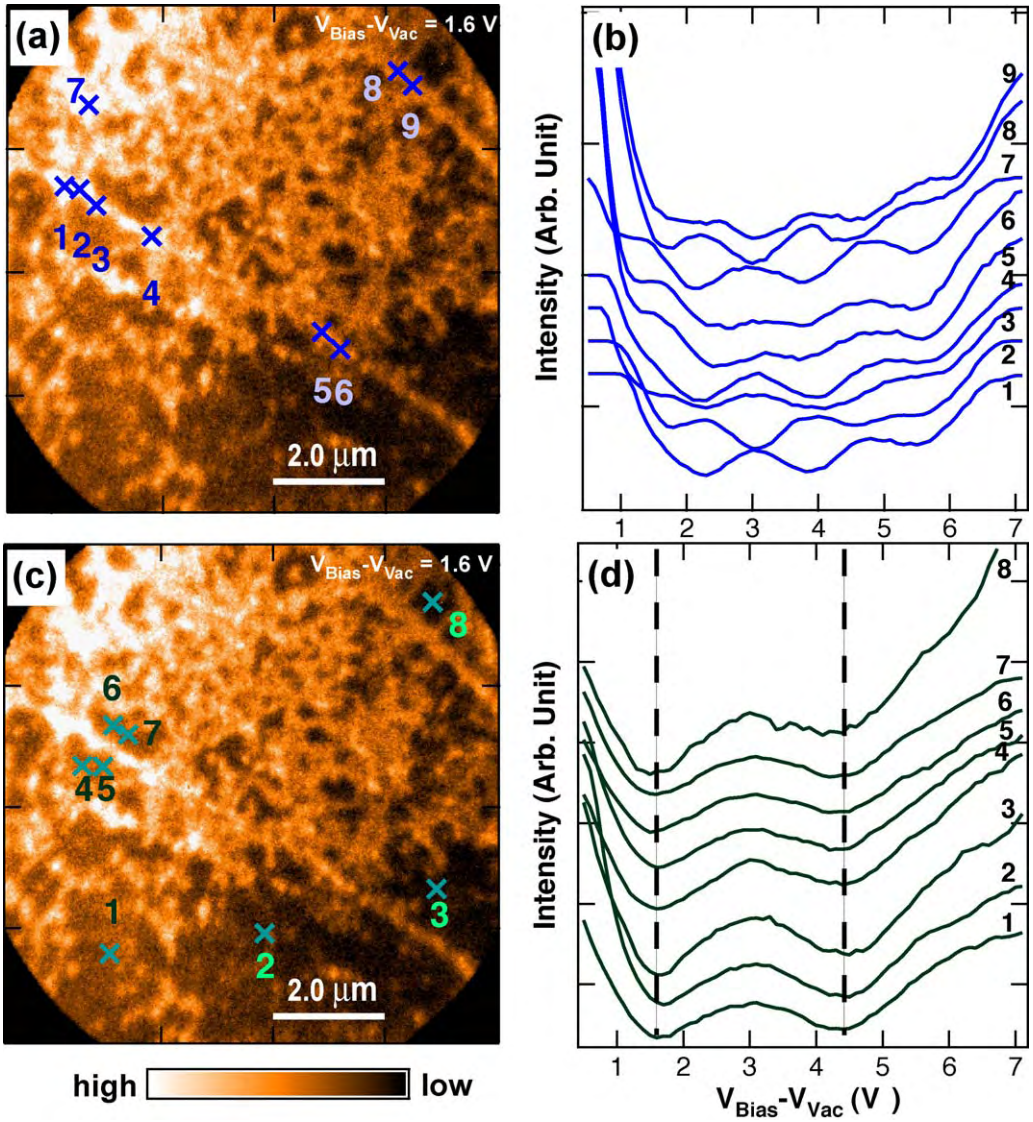

Fig. 2. IV-LEEM analysis of the graphene grown on the scratched SiC substrate at various positions labeled by numbers. (a) and (c) show the various analyzed positions on the scratch and away from the scratch respectively. (b) and (d) show corresponding IV plots of each labeled positions in (a) and (c) respectively. The IV oscillations indicate that there are mostly. 3–4 graphene layers on scratched locations and 2 graphene layers otherwise. The dashed lines in (d) are at the bias voltages where the image contrast between 2 graphene layers and higher number of layers is high.

graphitization process which will be described in the next paragraph. From the AFM measurement, scratches which occur during the polishing process (i.e. due to polishing substance) have widths and depths distributed mainly around two sets of values: (1) 120 nm wide and 1–2 nm deep, and (2) 230 nm wide and 5 nm deep. The scratch lengths are usually longer than 50 μm. Low energy electron microscopy (LEEM) and low energy electron diffraction (LEED) measurements were then performed in situ with a Elmitec LEEM III equipped hemisphere electron energy analyzer at Beamline 3.2b, Synchrotron Light Research Institute (SLRI), Thailand. The base pressure during measurement was 3×10^{-10} torr.

Before putting the SiC substrate in the vacuum chamber, the substrate was cleaned by (i) the mixture of NH_4OH, H_2O_2, and de-ionized water with a ratio of 1:1:5 as well as heated at 70 °C for 10 min, (ii) etched by 5% HF acid and (iii) the mixture of HCL, H_2O_2, and de-ionized water with a ratio of 1:1:5 as well as heated at 70 °C for 10 min. The substrate was then flashed to around 1200 °C by electron-beam bombardment 3 times in order to remove oxides from the surface. After the oxides were removed, we observed $6\sqrt{3} \times 6\sqrt{3}$ reconstruction of SiC in the LEED pattern; this indicates that the first carbon layer, the so called buffer layer [21], was formed. To reduce some scratches on the sample surface, the sample was heated to around 1300 °C while flowing purified hydrogen gas into the UHV chamber for 40 min with base pressure 1×10^{-7} torr and then the sample was flashed to 1400 °C. During these etching and flashing processes, the thermal decomposition of the substrate surface occurred and graphene was formed on the surface. LEEM images of graphene formed on the SiC substrate were measured at the field of view (FOV) of 25 μm, as shown in Fig. 1.

While some information regarding the surface topography can be obtained from the LEEM image, the LEEM technique can also determine the distribution of local graphene thickness by measuring a series of LEEM images at different incident-electron bias voltages (i.e. varying electron energy) [18,20,22–24]. Information on the number of graphene layers is contained in the oscillating intensity of reflecting electrons as a function of the voltage, i.e. I–V LEEM analysis [20,23]. In the I–V LEEM analysis, given a graphene thickness, electrons with only certain discrete energy levels are allowed inside the quantum well potential [20,25]. Due to these discrete energy levels, incident electrons with various energies

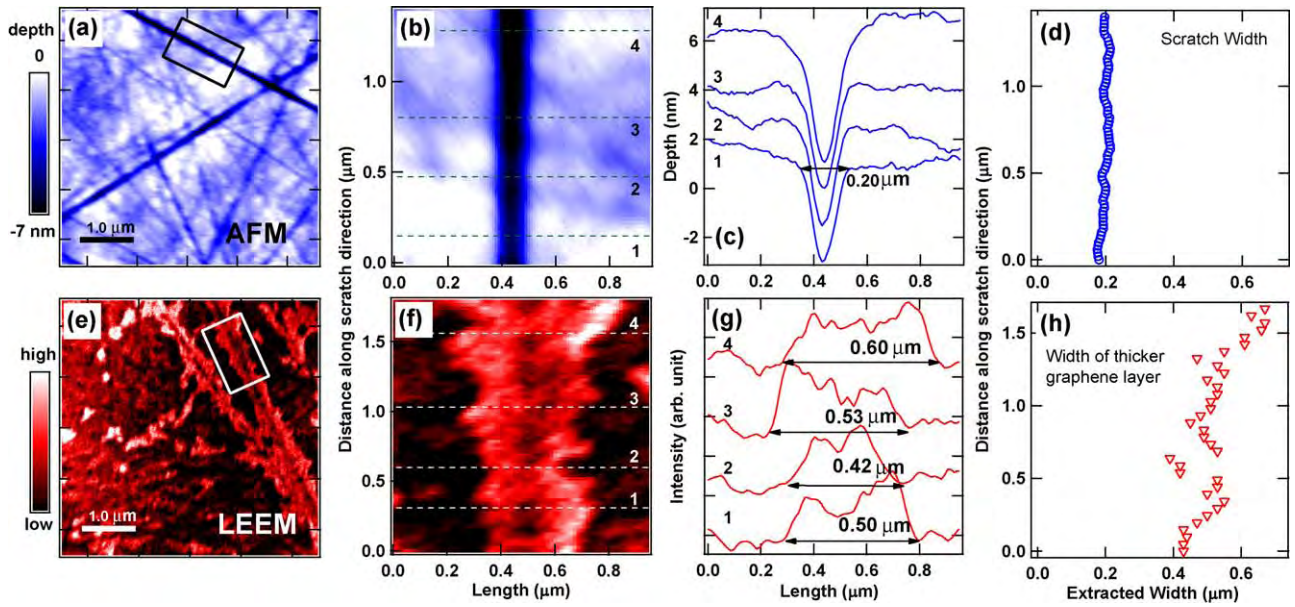

Fig. 3. Comparison of the scratch width and the width of the thicker graphene layer. (a) shows AFM image of SiC substrate before the graphitization process with 5 μm FOV where the color represents relative depth of the surface. (b) shows the magnified area of the black rectangle in (a). (c) shows the depth profiles corresponding to the dashed lines in (b) and (d) shows the full width along the scratch direction in (b). (e) shows the LEEM image of graphene on the SiC substrate after the graphitization process where the color represents LEEM intensity. The same procedures as (b)–(d) are applied to the LEEM image as shown in (f)–(h) to get the width of the thicker graphene layer, except that the width is obtained from the distance between the bottoms of the two leading edges.

will get reflected differently, creating an oscillating I–V spectrum which corresponds to the particular thickness. When the thickness of graphene layers changes, the oscillating I–V curve will change accordingly. We performed this I–V LEEM analysis on a set of LEEM images to determine the number of graphene layers at different locations in the sample as shown in Figs. 1 and 2.

3. Results and discussions

Fig. 1 shows the LEEM images taken after etching and flashing processes, with FOV of 25 μm. In Fig. 1(b), the scratch marks are mostly visible along high-intensity lines and the flat regions are mostly in low-intensity areas. However, these high and low intensities do not solely originate from the contrast of the surface topography since the LEEM technique also picks up the contrast from the electronic structure at the surface. As shown in Fig. 1(a)–(f), LEEM images are taken at the same spatial region while the adjusted bias voltage, $V_{Bias} - V_{Vac}$, is varied between 0–9 V where the voltages are 1.0, 1.6, 2.1, 3.0, 3.8 and 4.5 V respectively; note that V_{Vac} is defined as the vacuum energy level divided by electron charge, e [26]. As the electron energy is varied, the contrast of the LEEM image changes dramatically; at some energy (e.g. Fig. 1(c)), some of the scratch marks coming from the surface topography are barely visible. As briefly explained in Section 2, this change of the image intensity as a function of bias voltage is set by the electronic structure (i.e. quantum well states [20,25]) of graphene layers on SiC substrate. As shown in Fig. 1(g), the image intensities from the two selected spots (see blue and green squares in panel (a)–(f)) oscillate differently when the bias voltages vary in the same range as in Ref. [20]. The number of dips in this oscillation will equal the number of graphene layers at that spot [20,22,23]. The blue (green) curve has 4 (2) dips, indicating that there are 4 (2) layers of graphene on the selected blue (green) spot.

We have then applied this I–V LEEM method to various locations on LEEM images as shown in Fig. 2. In Fig. 2(a), spots labeled numbers 1–9 are selected from scratched areas and the corresponding I–V curves are then extracted and shown in panel (b). The numbers of dips are mostly 3–4, indicating that the numbers of graphene layers are mostly 3–4 in the scratched areas. On the other hand, in Fig. 2(d), the I–V curves selected from the smooth, low-intensity areas (spot numbers 1–8 in Fig. 2(c)) have mostly only two dips, indicating that the smooth areas are mostly covered with two layers of graphene. This data clearly suggests that scratches on the SiC surface can promote the enhanced growth of graphene. This behavior is similar to other studies [27–29] which show that the graphitization process usually starts near the steps of a surface rather than flat terraces. Ref. [29] describes "steps" on substrates as the kicker of graphene nucleation by providing C atoms. In our case, it is slightly different as a scratch has a wedge shape rather than a step shape; we observed that the enhanced growth of graphene happened not only right above the scratch areas but also extended significantly further from both edges of a scratch (see schematic picture in Fig. 4). Note that although we could not tell whether the additional layers are on top or underneath from our I–V LEEM analysis, we speculate that the additional layers are underneath based on the model in Ref. [27].

We then investigated further to what extent the enhanced graphene growth occurs away from the edges of a scratch. To measure the width of the scratches on the SiC substrate, we first performed AFM measurements before the graphitization process. The AFM image in Fig. 3(a) shows the relative depth at each spatial position; we then selected a portion of the scratch with a large width as shown in Fig. 3(b) which is the magnified area of the black rectangle in panel (a). The depth profiles along the perpendicular direction (e.g. dashed lines) are plotted in Fig. 3(c). The width along the scratch direction is then measured from the full width of these profiles, plotted in Fig. 3(d). We find that the average scratch width from this section is around 0.20 ± 0.01 μm. After the graphitization process, we performed the same procedure to the LEEM image of graphene on the SiC substrate (predominately within the white rectangle in panel (e)), as shown in Fig. 3(e)–(h). We note that for the LEEM image used for this analysis, we adjusted bias voltage so as to maximize the image contrast between the graphene domains in the vicinity of the scratches and the rest of the area (see the left vertical dashed line in Fig. 2(d), around $V_{Bias} - V_{Vac} = 1.6$ V). As shown in Fig. 3(h), the widths of graphene with more than

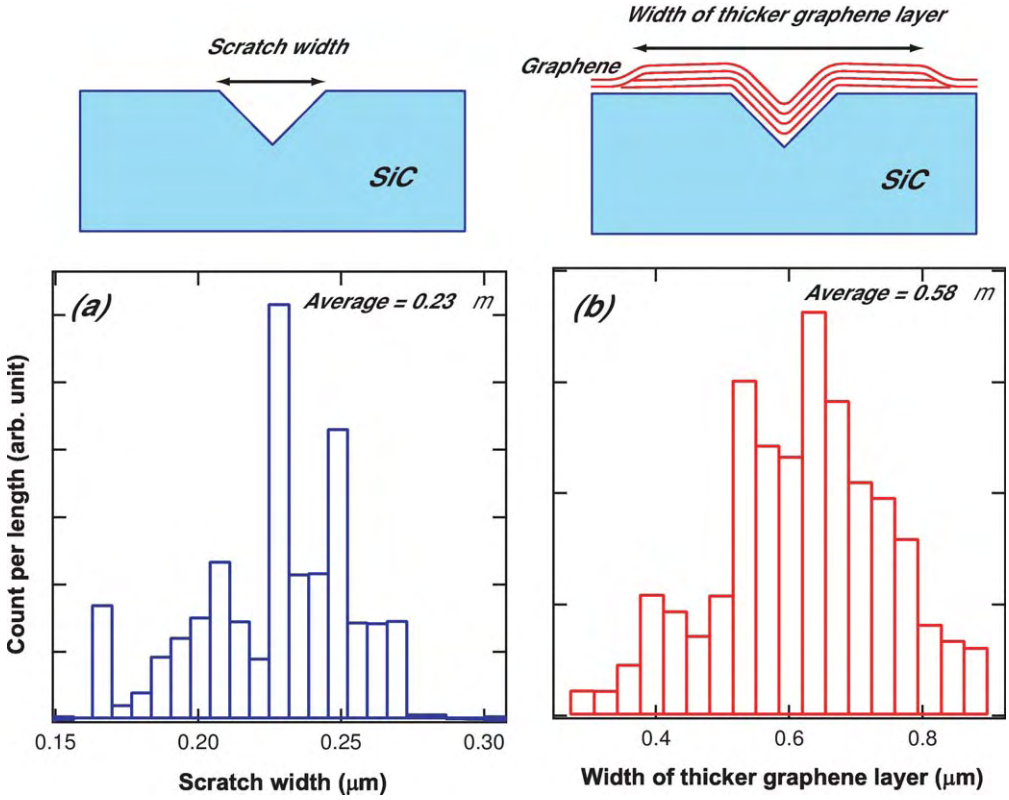

Fig. 4. (a) and (b) show the histograms of scratch widths extracted from various parts of AFM images and width of thicker graphene layer extracted from various parts of LEEM images, respectively. Above of the graphs are the schematic pictures of the widths measured from the scratch and the thicker graphene layers respectively.

2 layers, along the scratch direction, are extracted from the distance between bottoms of the two leading edges (see arrows in panel (g)). The average value of this width is around 0.52 ± 0.07 μm which is approximately 2.6 times larger than the average scratch width from Fig. 3(d).

Focused on other regions with large widths, we extracted more data from both AFM and LEEM images to get a better average. The histograms of these extracted widths are shown in Fig. 4. Note that these widths are measured along scratch direction with combined lengths of 20 μm and 30 μm from AFM and LEEM images, respectively (approximately 15 and 20 times longer length used in Fig. 3). The average scratch width is 0.23 μm and the average width of thicker graphene layer is around 0.58 μm which is approximately 2.5 times larger, similar to the ratio obtained in Fig. 3.

By comparing these extracted widths it is clear that the enhanced growth of graphene can extend much further from the edge of a scratch; see the schematic pictures in Fig. 4. This graphene formation near the wedge-shape groove appears to be different from the studies of graphene formed on [27,29,30] as these studies report that the thicker graphene layers usually occur within the two edges of the steps. Hence, the results of our investigation suggest that different shapes of surface discontinuities alter the formation of enhanced graphene growth in different ways. Although the microscopic origin is still subject to further investigation, this data already suggests a new method of using wedge-shape grooves to spatially vary the thickness of graphene formed on a SiC substrate.

4. Conclusion

By performing I–V LEEM analysis on graphene grown on SiC substrates, we find that the number of graphene layers is usually greater near scratched areas of SiC substrate. These thicker areas of graphene occur not only within the scratch itself but also extend significantly outwards from the edges of a scratch. From this case study, the width of the thicker graphene layers can be up to 2.5 times larger than the scratch width itself. While it would be interesting to investigate further on how to control this width, the current study already suggests an alternative way of using a scratch (i.e. wedge shape grooves) pattern for spatially varying graphene layers grown on a 6H–SiC(0 0 0 1) substrate.

Acknowledgments

W.M. would like to thank D. Ando for helpful support and comments. This study was supported by the Office of the Higher Education Commission, Thailand, under the program of Strategic Scholarships for Frontier Research Network and under NRU project of Thailand, and Suranaree University of Technology (SUT). W.M. acknowledges TRF–CHE–SUT for financial support.

References

[1] K.S. Novoselov, et al., Science 306 (2004) 666.
[2] A.K. Geim, K.S. Novoselov, Nat. Mater. 6 (2007) 183.
[3] K.S. Novoselov, et al., Science 315 (2004) 1379.
[4] A. Bostwick, et al., Science 328 (2010) 999.
[5] E.V. Castro, et al., Phys. Rev. Lett. 99 (2007) 216802.
[6] T. Ohta, et al., Phys. Rev. Lett. 98 (20) (2007) 206802.
[7] K.S. Novoselov, et al., PNAS 102 (2005) 10451.
[8] P.W. Sutter, et al., Nat. Mater. 7 (2008) 406.
[9] A. Siokou, et al., Appl. Surf. Sci. 257 (2011) 9785.
[10] K.S. Kim, et al., Nature 457 (2009) 706.
[11] J.L. Qi, et al., Appl. Surf. Sci. 257 (2011) 6531.
[12] A. Bostwick, et al., Nat. Phys. 3 (2007) 36.
[13] S.Y. Zhou, et al., Nat. Mater. 6 (2007) 770.
[14] X. Wu, et al., Appl. Phys. Lett. 95 (2009) 223108.
[15] J. Jobst, et al., Phys. Rev. B 81 (2010) 195434.
[16] K.V. Emtsev, et al., Nat. Mater. 8 (2009) 203.

[17] C. Virojanadara, et al., Surf. Sci. 603 (2009) L87.
[18] C. Virojanadara, et al., J. Phys. D: Appl. Phys. 43 (2010) 374010.
[19] C. Berger, et al., Science 312 (2006) 1191.
[20] H. Hibino, et al., Phys. Rev. B 77 (2008) 075413.
[21] I. Forbeaux, et al., Phys. Rev. B 58 (1998) 16369.
[22] C. Virojanadara, et al., Phys. Rev. B 78 (2008) 245403.
[23] H. Hibino, et al., Phys. Rev. B 80 (2009) 085406.
[24] P.J. Fisher, et al., J. Vac. Sci. Technol. A 28 (2010) 958.
[25] S. Bose, et al., N. J. Phys. 12 (2010) 023028.
[26] H. Hibino, et al., e-J. Surf. Sci. Nanotechnol. 6 (2008) 107–110.
[27] W. Norimatsu, M. Kusunoki, Phys. E 42 (2010) 691.
[28] J. Choi, et al., J. Phys. Chem. C 114 (2010) 13344–13348.
[29] S. Tanaka, et al., Phys. Rev. B 81 (2010) 041406.
[30] M. Sprinkle, et al., Nat. Nanotechnol. 5 (2010) 727.

เอกสารที่ 4

W. Meevasana*, X.J. Zhou, B. Moritz, C.-C. Chen, R.H. He, S.-I. Fujimori, D.H. Lu, S.-K. Mo, R.G. Moore, F. Baumberger, T.P. Devereaux, D. Van Der Marel, N. Nagaosa, J. Zaanen, Z.-X. Shen, “Strong energy-momentum dispersion of phonon-dressed carriers in the lightly doped band insulator $SrTiO_3$”, *New Journal of Physics* 12, 23004 (2010)

New Journal of Physics
The open-access journal for physics

Strong energy–momentum dispersion of phonon-dressed carriers in the lightly doped band insulator $SrTiO_3$

W Meevasana[1,2,3,4,12], X J Zhou[5], B Moritz[2], C-C Chen[1,2], R H He[1,2], S-I Fujimori[6], D H Lu[2], S-K Mo[1,7], R G Moore[2], F Baumberger[3], T P Devereaux[2], D van der Marel[8], N Nagaosa[9,10], J Zaanen[11] and Z-X Shen[1,2]

[1] Departments of Physics and Applied Physics, Stanford University, CA 94305, USA
[2] Stanford Institute for Materials and Energy Sciences, SLAC National Accelerator Laboratory, 2575 Sand Hill Road, Menlo Park, CA 94025, USA
[3] School of Physics and Astronomy, University of St. Andrews, North Haugh, St. Andrews, Fife KY16 9SS, UK
[4] Synchrotron Light Research Institute, Nakhon Ratchasima 30000, Thailand
[5] Institute of Physics, Chinese Academy of Sciences, Beijing 100190, People's Republic of China
[6] Synchrotron Radiation Research Unit, Japan Atomic Energy Agency, Mikazuki, Hyogo 679-5148, Japan
[7] Advanced Light Source, Lawrence Berkeley National Lab, Berkeley, CA 94720, USA
[8] Département de Physique de la Matière Condensée, Université de Genève, quai Ernest-Ansermet 24, CH1211, Genève 4, Switzerland
[9] Department of Applied Physics, The University of Tokyo, Bunkyo-ku, Tokyo 1138656, Japan
[10] Cross-Correlated Materials Research Group (CMRG), ASI, RIKEN, Wako 351-0198, Japan
[11] The Instituut-Lorentz for Theoretical Physics, Leiden University, Leiden, The Netherlands
E-mail: wm14@st-andrews.ac.uk

New Journal of Physics **12** (2010) 023004 (11pp)
Received 10 October 2009
Published 3 February 2010
Online at http://www.njp.org/
doi:10.1088/1367-2630/12/2/023004

[12] Author to whom any correspondence should be addressed.

Abstract. Much progress has been made recently in the study of the effects of electron–phonon (el–ph) coupling in doped insulators using angle-resolved photoemission (ARPES), yielding evidence for the dominant role of el–ph interactions in underdoped cuprates. As these studies have been limited to doped Mott insulators, the important question arises as to how this compares with doped band insulators where similar el–ph couplings should be at work. The archetypical case is that of perovskite $SrTiO_3$ (STO), well known for its giant dielectric constant of 10 000 at low temperatures, exceeding that of La_2CuO_4 by a factor of 500. Based on this fact, it has been suggested that doped STO should be the archetypical bipolaron superconductor. Here we report an ARPES study from high-quality surfaces of lightly doped STO. In comparison to lightly doped Mott insulators, we find the signatures of only moderate el–ph coupling; a dispersion anomaly associated with the low-frequency optical phonon with a $\lambda' \sim 0.3$ and an overall bandwidth renormalization suggesting an overall $\lambda' \sim 0.7$ coming from the higher frequency phonons. Furthermore, we find no clear signatures of the large pseudogap or small-polaron phenomena. These findings demonstrate that a large dielectric constant itself is not a good indicator of el–ph coupling and highlight the unusually strong effects of the el–ph coupling in doped Mott insulators.

Contents

1. Introduction

The notion that carriers doped into insulators get dressed by lattice deformations has been around for a long time [1, 2]. A recent development is that this polaron formation can be studied experimentally using angle-resolved photoemission (ARPES), yielding more direct information on the physics than classical transport and optical spectroscopic methods. Especially when the carrier density is small but finite, where a controlled theoretical framework is lacking, ARPES has been quite revealing. The case has been made that lightly doped cuprates fall victim to small-polaron formation (strong interacting case) that is vulnerable to self-trapping by impurities [3, 4]; in undoped cuprates, the spectral functions reveal Frank–Condon-type broad humps caused by the coupling to multiple phonons, and only when doping is increased does a well-defined quasi-particle (QP) peak start to emerge [3, 4]. Another recent ARPES revelation is found in the context of highly doped manganites in the colossal magnetoresistance regime. At high temperatures ARPES reveals the Frank–Condon humps signaling small polarons, while upon lowering temperature small pole-strength QP peaks appear in addition, indicating that a coherent Fermi liquid is formed from the microscopic polarons [5].

Both manganites and cuprates are doped Mott insulators and no modern ARPES information is available on polaron physics in the simpler doped band insulators. We therefore decided to focus on the classic $SrTiO_3$ (STO) doped band insulator. STO is known to have an exceptionally high static dielectric constant on the order of 10^4 at low temperatures [6]. Superconductivity can be induced by electron doping with O, Nb or La [7, 8] over a narrow range of low carrier concentrations between $\sim 10^{19}$ and $\sim 10^{20}\,\mathrm{cm}^{-3}$. Optimal T_c is typically 0.2–0.3 K but can reach up to 1.2 K [9], which is surprisingly high for such low carrier concentrations. It has been speculated that this is due to the formation of bipolarons [10]. However, whether large or small polarons actually exist in STO depends on the relevant length scale for the electron–phonon (el–ph) couplings.

The case was made in a recent optical study by van Mechelen *et al* that el–ph coupling is actually not very strong [11]. ARPES is, however, more direct in revealing the strength of coupling to specific phonons. With this technique we arrive at the conclusion that small polarons are not formed in STO and that el–ph coupling acts in a perturbative way.

2. Methods and materials

The samples investigated here are $La_xSr_{1-x}TiO_{3+\delta}$ (Crystal Base Co., Japan) at nominal dopings of $x = 0.01$ ($T_c \sim 0.2$ K) and $x = 0.05$ (non-superconducting) [8] while the actual doping levels at the surface are slightly different due to oxygen vacancies. We obtain high-quality surfaces by cleaving along guiding lines at $T = 10$ K and measure at the same temperature. This new technique results in significantly flatter surfaces than when fracturing or scraping STO. This was found to substantially improve the quality of ARPES data and enable us to see a clear QP band dispersion and dispersion anomaly, which have not been seen in previous measurements [12]–[14].

ARPES data were collected on a Scienta-4000 analyzer at the Stanford Synchrotron Radiation Laboratory, Beamline 5–4, and the Advanced Light Source (ALS), Beamline 10.0.1, with photon energies between 18 and 90 eV and a base pressure of $<4 \times 10^{-11}$ Torr. Samples were cleaved *in situ* along the (001) plane at the measurement temperature, $T = 10$ K. A sharp (1×1) low-energy electron-diffraction pattern indicates a well-ordered surface devoid of any reconstructions. The energy resolution was set to 9–11 and 15–20 meV for 18–35 and 35–90 eV photon energies, respectively, and the angular resolution was 0.35°. Additionally, an LSCO sample with $x = 0.01$ was measured at ALS with photon energy = 55 eV and $T = 20$ K.

3. Results

In figure 1, we present ARPES data taken at a photon energy of 27 eV. The dominant features in the angle-integrated spectrum are the valence band between 3.3 and 9 eV, an in-gap state near 1.3 eV and the QP peak at the Fermi level. The energy gap between the onset of the oxygen valence bands to the QP band bottom is around 3.3 eV, consistent with optical measurements [15], while local-density-approximation (LDA) band structure calculations predict a gap of ~ 2 eV [14, 16]. The presence of a non-dispersive and broad in-gap state around 1.3 eV has been discussed in the literature ([13] and references therein) as caused by a local screening effect, chemical disorder or donor levels.

Having established the basic spectral features, we now focus on the Fermi surface topography of STO. Figures 2(a)–(d) show ARPES data taken at various photon energies

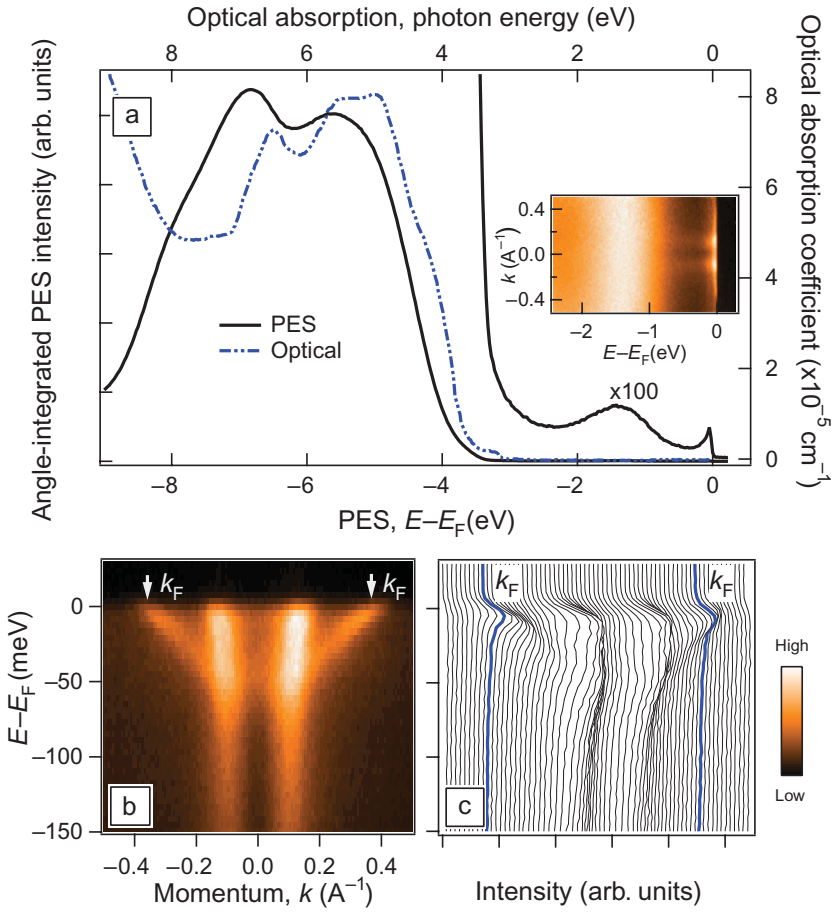

Figure 1. ARPES data of the $x = 0.01$ sample at $T = 10$ K. (a) Angle-integrated photoemission spectrum up to 9 eV in binding energy, together with optical absorption data of an undoped sample from [15]. The inset shows angle-resolved data of the in-gap state around 1.3 eV. (b) QP band dispersion in the (010) plane near E_F (see cut b in figure 2(f)) with corresponding energy distribution curves (EDCs) in (c).

(changing k_z) together with a Fermi surface map at 27 eV, projected on the k_x–k_y plane (figure 2(e)). The flatter band with an ~60 meV band bottom (i.e. in figures 2(a)–(c)) corresponds to a bulk state since the k_F crossing changes with different photon energy (changing k_z), in agreement with LDA calculations by I I Mazin where the computational details are the same as in [11]. The steeper band with an ~200 meV bottom (e.g. in figure 2(d)) can be attributed to the surface of cleaved STO because the data do not show noticeable dispersion along k_z and they are absent in LDA calculations (indicated by the blue line and surface in figures 2(e) and (f)). Since the surface band crosses the bulk band, it cannot be an eigenstate of the system but possibly a surface resonance state; this surface state is investigated further in smaller doping, $x = 0.001$ samples [17]. We also note that in $x = 0.01$ samples a second bulk band is expected with a Fermi crossing near the surface band. However, this band appears to be overshadowed by the more intense surface-related band and further suppressed by the matrix element near the Γ point. In the following, we will use the schematic contours of the k_F positions, indicated by green surfaces in figure 2(f), to describe the bulk Fermi surface.

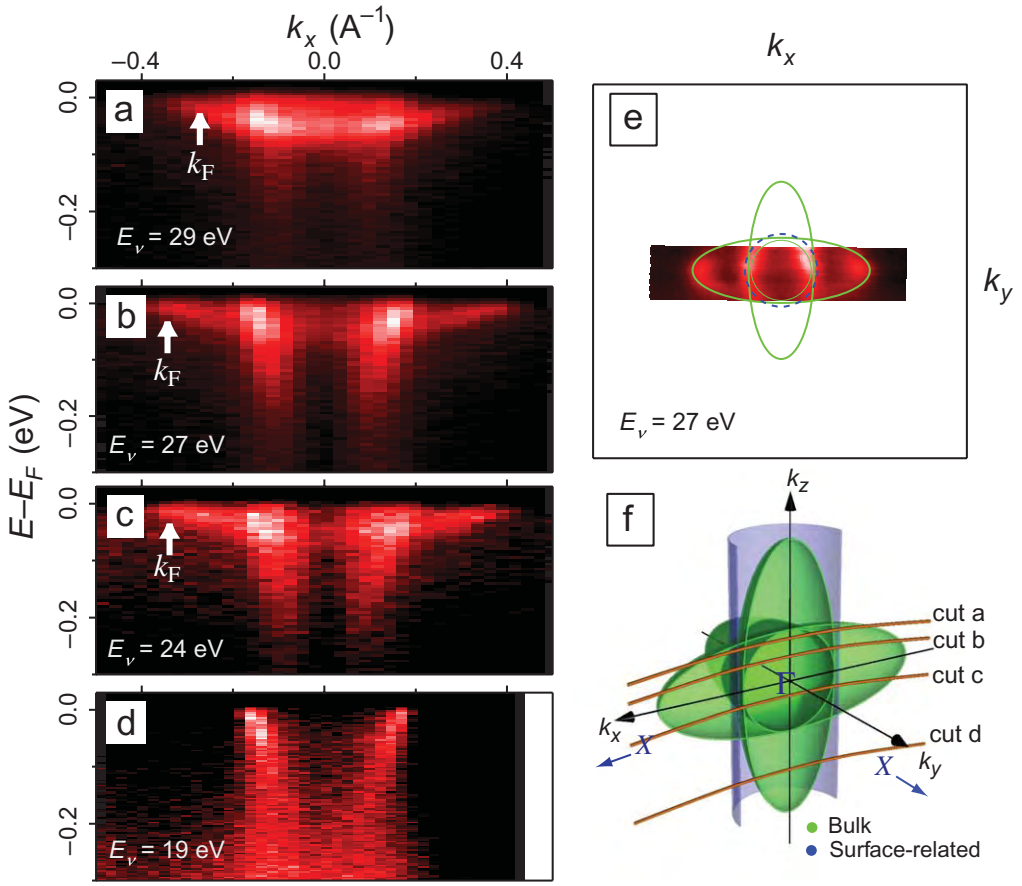

Figure 2. Fermi surface topography of STO. (a)–(d) Band dispersion in the (010) plane for photon energies of 19, 24, 27 and 29 eV, respectively. Doped STO has a cubic unit cell and a three-dimensional Fermi surface, consisting of three ellipsoid-like surfaces along each axis (see more details in [14]); when including the spin orbit coupling term in the calculation [11], a shift in the Fermi surface occurs, as shown in figure 3(e). (e) Fermi surface map near the Brillouin zone mid-plane ($h\nu = 27$ eV). The solid green lines are guides to the eye. Estimated k_z positions for (a)–(d) are indicated by the orange lines in the schematic Fermi surface (f), where half of the whole Fermi surface is plotted; green (blue) indicates the bulk (surface) band. Note that in $x = 0.01$ samples a second bulk band is expected with a Fermi crossing near the surface band. However, this band appears to be overshadowed by the more intense surface-related band and further suppressed by the matrix element near the Γ point.

Figures 3(a) and (b) show the occupied bands, along the ΓX direction in the vicinity of the Γ point of the $x = 0.01$ and 0.05 samples. By aligning the k_Fs of the ARPES data with those of the LDA dispersions [11], we estimate that the dopings of the $x = 0.01$ and 0.05 samples are slightly higher than the nominal dopings (1.5 ± 0.2 and 5.6 ± 0.5%, respectively: figure 3(e)), likely due to a small oxygen deficiency at the surface.

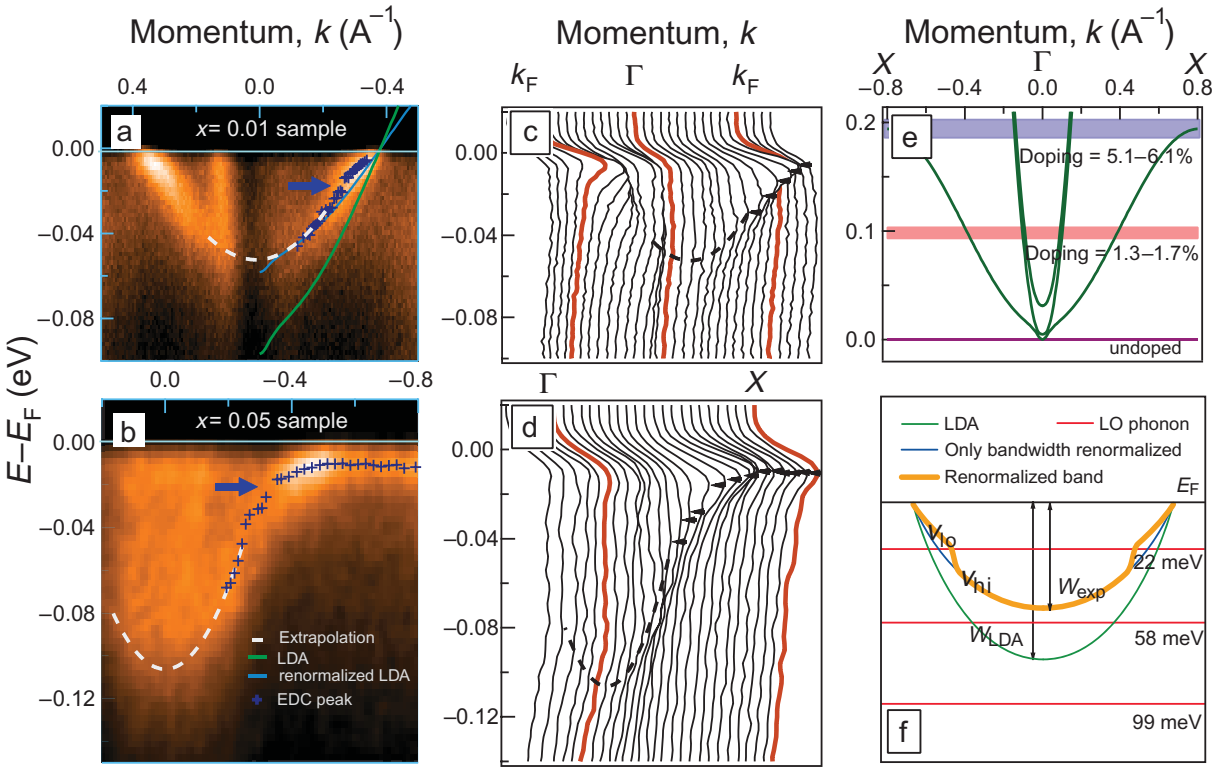

Figure 3. (a), (b) QP band dispersions of the $x = 0.01$ and 0.05 samples. Cross symbols indicate peaks from EDCs and dashed lines are extrapolated to obtain the band bottom. The most prominent kink energy is indicated by arrows around $\sim$20 meV for both doped samples. Possibly, there is a second kink in the $x = 0.05$ sample between 40 and 60 meV, but the complication from the side band makes it less clear. Note that k_z varies slightly along the k-axis of (a) and (b) (see figure 2). However, this change has only a minute influence on the measured group velocities and will be neglected for the discussion of mass renormalization. (c) and (d) show EDCs of ARPES data shown in (a) and (b), respectively, where the EDC peak positions are marked by triangle symbols and the dash lines are extrapolations. (e) LDA band dispersion of undoped STO along ΓX [11]. Fermi levels positions for dopings = 1.3–1.7 and 5.1–6.1% are indicated by shaded areas. (f) Schematic plot of renormalized band dispersion in the forms of 'kink' and reduced bandwidth caused by phonons whose mode energies are lower and higher than the electron bandwidth, respectively.

Having isolated the occupied part of the conduction bands (figures 3(a)–(d)), let us now turn to interpretation of the data. In the data one can discern a weak kink in the dispersion at approximately 20 meV binding energy (blue arrows, figures 3(a) and (b)). This is clear in the $x = 0.01$ sample, since in the $x = 0.05$ sample it resides in a region where the dispersion has a strong curvature (figure 3(e)). Such a weak kink structure in the dispersion indicates a perturbative coupling with a bosonic mode at this energy. This interpretation is supported by the observation that the intensity rapidly increases below the kink energy; above the kink energy, an extra decay channel that will smear the QP peak opens up. To quantify the coupling to

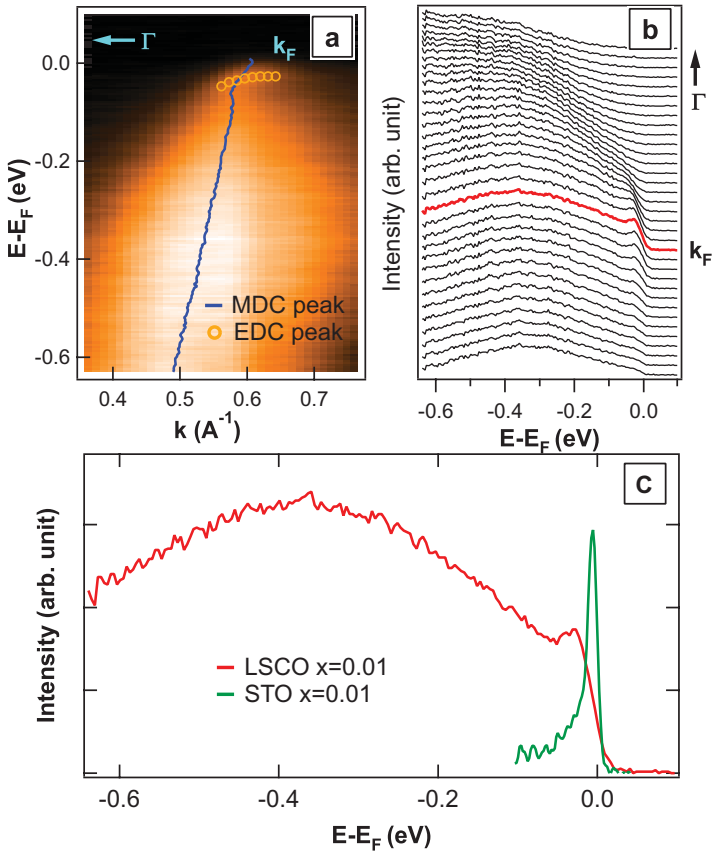

Figure 4. ARPES data of $La_{1-x}Sr_xCuO_4$ with $x = 0.01$. (a) Raw ARPES data; the blue line indicates the peak position in momentum distribution curves and orange circles indicate the peak positions in EDCs where the big arrow indicates the kink in dispersion at binding energy ∼70 meV. (b) Corresponding EDCs. (c) Comparison of ARPES spectra with background subtracted at k_F of (1) $x = 0.01$ STO sample along the $\Gamma - X$ direction and (2) 1% doping $La_{2-x}Sr_xCuO_4$ along the (0, 0) to (π, π) direction.

this boson, we extracted the band velocities for the $x = 0.01$ case at binding energies below (v_{lo}) and above (v_{hi}) the kink energy (see figure 3(f)) to be ∼0.16 and 0.21 eV Å, respectively. Mass renormalization is therefore $v_{hi}/v_{lo} = m^*/m \sim 1.3$, indicating a coupling to this particular boson, $\lambda' \equiv m^*/m - 1 = 0.3$.

Given that the signals are somewhat smeared at higher energies, we cannot exclude the presence of other kinks associated with higher energy modes. However, the data permit us to track the overall width of the occupied parts of the conduction bands. For the $x = 0.01$ sample we find the band bottom at ∼58 meV, whereas the LDA calculation indicates it to be at ∼97 meV [11] (figure 3(e)). It follows that the overall width of the occupied band is renormalized by a factor of ∼1.7 (W_{LDA}/W_{exp}). The total mass renormalization is the product of the bandwidth and kink renormalization factors and we find this to be $1.7 \times 1.3 \simeq 2.2$ in the $x = 0.01$ sample, close to the estimate 2–3 deduced from the optical measurements [11].

To compare with STO data, figure 4 shows ARPES data of $La_{1-x}Sr_xCuO_4$ with $x = 0.01$, as a lightly doped Mott insulator. The momentum is along the (0, 0) to (π, π) direction. We

note that all the data in figure 4 are already subtracted by the non-dispersive background of the oxygen valence band for clearer comparison. In contrast to STO, the spectrum (see the red line in figure 4(b)) shows a small QP peak with a large Frank–Condon-type broad hump around 400 meV—a signature of small-polaron formation. LSCO data also show a clear kink in the dispersion, indicating strong el–ph coupling at around 70 meV (see the arrow in figure 4(a)); to quantify this coupling, we extracted the band velocities at binding energies below ($v_{\rm lo}$) and above ($v_{\rm hi}$) the kink energy to be $\sim$1.66 and 6.14 eV Å, respectively. Therefore, the mass-renormalization factor from this kink feature is $v_{\rm hi}/v_{\rm lo} = m^*/m \sim 3.7$. The use of $\lambda' \equiv m^*/m - 1$ would give a λ' of 2.7, indicating a clear contrast to the extracted value of $\sim$0.3 from the kink feature of the $x = 0.01$ STO sample.

4. Discussion and conclusion

How does one interpret these findings from STO data? The 20 meV kink is certainly related to a phonon. *A priori* one can be less certain about the cause of overall bandwidth renormalization because an electronic origin cannot be excluded. However, although LDA is known to underestimate band gaps in band insulators, it does not usually underestimate the bandwidths and our extracted renormalization factor may be regarded as an upper value. At the same time, the phonon dispersions of STO have been measured by infrared and Raman spectroscopy [15] and neutron scattering [18]–[21] in great detail; the phonon modes are in the range of 0–100 meV where much of the phonon spectrum extends to energies that are larger than the Fermi energy of at least the $x = 0.01$ system. Under such an anti-adiabatic condition, one expects the el–ph coupling to give rise to an overall bandwidth renormalization that can be estimated from the mass-renormalization formulae for the isolated polaron [1]. Since the focus here is on the surprisingly moderate el–ph coupling, we attribute all the renormalization to el–ph interaction, which sets the upper bound for the value of $\lambda \sim 1$. An overall coupling $\lambda \sim 1$ can mean that small, self-trapped polarons are formed but also that the system stays itinerant. What decides the nomenclature is the length scale of the relevant el–ph couplings.

When the el–ph coupling is short ranged, small polarons are expected. One can take the cuprates as an example where an effective $\lambda \simeq 1$ corrected for electronic band narrowing effects [22] that enhance the impact of el–ph interaction is believed to be responsible for the multi-phonon Franck–Condon peak indicated in figure 4(c). Here we should note that m^* is no longer linear with λ and increases rapidly near the small-to-large polaron crossover around $\lambda \simeq 1$. For $\lambda \simeq 1$ in cuprates (e.g. in the case of LSCO shown in figure 4), the actual face value of mass renormalization could be as large as 3.7; hence, λ' defined by $m^*/m - 1$ would be 2.7.

The most striking aspect of the STO data is that such effects due to small-polaron formation are entirely absent in STO, where instead the electrons remain strongly coherent as manifested by the strong energy–momentum dispersion and the distinctly sharp QP peaks with large pole strengths even for the 1% doped sample (figure 4(c)). This can be reconciled with the relatively large λ, assuming that the dominating el–ph couplings are of the long-range, polar kind [23]. This claim can in fact be further substantiated by the finding that our data are in semi-quantitative agreement with 'naive' continuum limit estimations of the polar el–ph interactions [10, 24]. In this way, only the long-range electrostatic interactions are taken into account with the longitudinal optical (LO) phonons, omitting completely short-range interactions involving the transversal optical (TO) phonons that are, in reality, always present.

Table 1. Comparison of features between STO and cuprate—perovskite band and Mott insulators.

Feature	Mott insulator (La_2CuO_4)	Band insulator (STO)
Mass renormalization factor from the kink feature at small doping $x = 0.01$	∼3.7	∼1.3
Small polaronic effect at small doping	Yes	No
Large pseudogap behavior at small doping	Yes	No
Small Fermi surface pocket at small doping	Maybe (YBCO) [27]	Yes
Dielectric constant (undoped)	∼20 [28]	$\sim 10^2 - 10^4$

Starting from this perspective, let us first discuss why the large bulk dielectric constant may not be a good indicator for the formation of small polarons. The dielectric constants at zero frequency (ε_0) and at frequencies large by comparison to the phonon energy (ε_∞) are related to the frequencies of LO and TO phonons as $\varepsilon_0/\varepsilon_\infty = \Pi_a(\omega_{a\mathrm{LO}}/\omega_{a\mathrm{TO}})^2$, where a specifies the phonon branch. A large ε_0 signals a softening of the TO phonon that eventually can condense in a ferroelectric state. However, the Fröhlich polar el–ph interactions involve the LO phonons, where the large ε_0 will also help the coupling strength but with smaller effect. The coupling strength depends on the dielectric term $\kappa^{-1} = \varepsilon_\infty^{-1} - \varepsilon_0^{-1}$, which increases slightly upon increase of ε_0 ($\kappa^{-1} \sim 0.17$ in La_2CuO_4 and ∼0.19 in STO) [25]. Another issue is that the short-range coupling to this TO phonon could be enhanced due to the softening of the frequency ω_{TO}. However, since the softening occurs only in a narrow region in momentum space characterized by the scale $a/\xi \cong 0.1$ (ξ is the correlation length) [19, 20], the increase in the coupling constant $\Delta\lambda$ of the order of $\Delta\lambda \cong \lambda(\omega_{\mathrm{TO}}^0/\omega_{\mathrm{TO}})^2(a/\xi)^3$ is small.

Under these assumptions, one is, according to the calculations of Devreese *et al* [10, 24], left with three LO phonons at (for $q = 0$) 22, 58 and 99 meV with coupling constants α_i of 0.018, 0.945 and 3.090, respectively. Using that, for weak coupling, $\lambda_i = \alpha_i/6$ [1, 26] this translates into λ_i's of 0.003, 0.16 and 0.6, respectively. These modes are indicated together with the electronic dispersions in the schematic figure 3(f). The low-energy kink in the electron dispersions matches very well the 22 meV mode associated with Sr–O bond stretching [21]. The other two phonon modes are at higher energy than the band bottom and hence should cause an overall bandwidth reduction. For an accurate treatment, one may consider the anti-adiabatic limit; however from the available calculation, the coupling constants α of these 58 and 99 meV modes will give a bandwidth-renormalized factor of 1.76, which is already very close to our extracted value of ∼1.7. The polar el–ph calculation strongly underestimates the $\lambda' \simeq 0.3$ coupling to the 22 meV phonon. The main coupling from this Sr–O bond stretching mode comes from large momenta near the zone boundary as in the cuprates, and is expected

from general grounds due to the displacement eigenvectors. Thus, it is a local deformation. As discussed in the previous paragraph, this could well be significantly enhanced by proximity to the ferroelectric transition, one reason why its main impact is only on the low-energy phonon. However, given that the coupling is still moderate and this phonon is of the adiabatic/Eliashberg kind, it does not interfere with the consistency of our argument.

While small polarons are absent in STO, cuprates at similar doping show a sharp contrast in displaying strong el–ph coupling with mass renormalization as large as 3.7 (see table 1 for the comparison between LSCO and STO). For the following reasons, the carriers doped into a Mott insulator can be subject to a stronger short-range el–ph interaction. One reason is that the additional polaronic effect due to the magnetic degrees of freedom enhances the effective mass, and hence collaborate to form the composite small polaron with magnon and phonon clouds [29]. Another reason is that fluctuations with large momentum (e.g. $k = (\pi/2, \pi/2)$ of the antiferromagnetic state in the cuprates) are involved in dressing the doped carriers. Starting from the Fröhlich interaction, the exchange of this large momentum can lead to the short-range el–ph interaction. In the case of a band insulator, the large momentum in this same order of magnitude is not immediately available. Therefore, small-polaron formation is more likely to occur in a Mott insulator than in a band insulator. We should note that there could be an additional advantage in anisotropic layer compounds in that el–ph coupling along the perpendicular axis is little screened and hence remains strong [30, 31]. However, it is also known in cuprates that the small-polaron effect disappears largely upon doping away from the antiferromagnetism (e.g. $Na_xCa_{2-x}CuO_2Cl_2$ with $x = 0.12$ [3]), where the conductivity is still very anisotropic. Therefore, it is likely that there are also other physics (e.g. as discussed above) involved in helping the formation of small polarons.

In conclusion, we have shown the quite unexpected result that there is little evidence for small-polaron formation in lightly doped STO, indicating that the large dielectric behavior can occur independently of strong el–ph interactions. In turn, this indicates that in doped Mott insulators like the cuprates, the dressing of electrons by spin excitations [22, 29] and strong correlations combine to give a short-range el–ph interaction that is able to trap doped carriers and more readily form polarons.

Acknowledgments

We gratefully thank II Mazin for providing the unpublished LDA calculations, A Mishchenko for helpful discussion and H Takagi and J Matsuno for crystal information. This work was supported by the Department of Energy, Office of Basic Energy Sciences under contract DE-AC02-76SF00515. WM acknowledges The Thailand Research Fund for financial support. CCC was supported in part by National Science Council, Taiwan, under grant no. NSC-095-SAF-I-564-013-TMS.

References

[1] Devreese J T and Alexandrov A S 2009 *Rep. Prog. Phys.* **72** 066501
[2] Alexandrov A S and Mott N F 1994 *Rep. Prog. Phys.* **57** 1197
[3] Shen K M *et al* 2004 *Phys. Rev. Lett.* **93** 267002
[4] Yoshida T *et al* 2003 *Phys. Rev. Lett.* **91** 027001
[5] Mannella N *et al* 2005 *Nature* **438** 474

[6] Muller K A and Burkard H 1979 *Phys. Rev.* B **19** 3593
[7] Koonce C S *et al* 1967 *Phys. Rev.* **163** 380
[8] Suzuki H *et al* 1996 *Phys. J. Soc. Japan* **65** 1529
[9] Bednorz J G and Muller K A 1988 *Rev. Mod. Phys.* **60** 585
[10] Verbist G, Peeters F M and Devreese J T 1992 *Ferroelectrics* **130** 27
[11] Van Mechelen J L M *et al* 2008 *Phys. Rev. Lett.* **100** 226403
[12] Imada M, Fujimori A and Tokura Y 1998 *Rev. Mod. Phys.* **70** 1039
[13] Ishida Y *et al* 2008 *Phys. Rev. Lett.* **100** 056401
[14] Aiura Y *et al* 2002 *Surf. Sci.* **515** 61
[15] Cardona M 1965 *Phys. Rev.* A **140** 651
[16] Luo W *et al* 2004 *Phys. Rev.* B **70** 214109
[17] Meevasana W *et al* unpublished work
[18] Cowley R A 1964 *Phys. Rev.* A **134** 981
[19] Shirane G and Yamada Y 1969 *Phys. Rev.* **177** 858
[20] Shirane G 1974 *Rev. Mod. Phys.* **46** 437
[21] Choudhury N *et al* 2008 *Phys. Rev.* B **77** 134111
[22] Rosch O *et al* 2005 *Phys. Rev. Lett.* **95** 227002
[23] Toyozawa Y 2003 *Optical Processes in Solids* (Cambridge: Cambridge University Press) pp 149–87
[24] Eagles D M 1965 *Phys. J. Chem. Solids* **26** 672
[25] Alexandrov A S and Bratkovsky A M 2000 *Phys. Rev. Lett.* **84** 2043
[26] Feynman R P 1955 *Phys. Rev.* **97** 660
[27] Doiron-Leyraud N *et al* 2007 *Nature* **447** 565
[28] Tamasaku K *et al* 1992 *Phys. Rev. Lett.* **69** 1455
[29] Mishchenko A S and Nagaosa N 2004 *Phys. Rev. Lett.* **93** 036402
[30] Alexandrov A S 1996 *Phys. Rev.* B **53** 2863
[31] Meevasana W *et al* 2006 *Phys. Rev. Lett.* **96** 157003

เอกสารที่ 5

S. Suwanwong, T. Eknapakul, C. Masingboon, P. Buaphet, S. Rattanasuporn, R. Pattanakul, H. Nakajima and **W. Meevasana***, "UV Irradiation Effect on Electrical Conductivity of $KTaO_3$ Crystals", *Proceedings of Siam Physics Congress SPC2012*, pp 213-215 (2012)

UV Irradiation Effect on Electrical Conductivity of $KTaO_3$ Crystals

S. Suwanwong[1], T. Eknapakul[1], C. Masingboon[1,2], P. Buaphet[1], S.Rattanasuporn[3], R. Pattanakul[3], H. Nakajima[3] and W. Meevasana[1, 3, 4*]

[1]*School of Physics, Institute of Science, Suranaree University of Technology, Nakhon Ratchasima, 30000, Thailand*
[2]*Faculty of Science & Engineering, Kasetsart University, Chalermphrakiat Sakorn-Nakorn Campus, Sakorn Nakorn, 47000, Thailand*
[3]*Synchrotron Light Research Institute, Nakhon Ratchasima, 30000, Thailand*
[4]*Thailand Center of Excellence in Physics, CHE, Bangkok, 10400, Thailand*
**Corresponding author. E-mail: worawat@g.sut.ac.th*

Abstract

Many light-sensing devices exploit the property of semiconducting materials such that their conductivity could change upon light exposure. The materials commonly used for these sensors have small band gaps and are not transparent under visible light. Here we are interested in the relatively-wide-band-gap material, $KTaO_3$. By using lithography technique for making sample electrodes, we found that the conductivity of insulating $KTaO_3$ single crystals could change dramatically upon exposing to focused sunlight. When there was no light, the resistance of $KTaO_3$ was high in order of GΩ (e.g. ~9 GΩ) but when we focused sunlight on the sample, the resistance could become much lower in order of MΩ (e.g. ~3 MΩ) or approximately 3 orders of magnitude lower. This indicates that the $KTaO_3$ could be used as a high-efficiency light sensing device. We will also discuss about our study using synchrotron light.

Keyword: $KTaO_3$, Light sensing Device, UV Irradiation Effect

Introduction

Light sensor devices which are photo-resistor, photo-cell, and photo-diode types have the same property that their conductivity could change upon light exposure. The materials commonly used for these sensors have small band gaps and are not transparent under visible light, such as CdS and CdSe (band gaps are 2.42 and 1.73 eV respectively [1, 2]. CdS and CdSe sensors are active in the wavelength range of 500-700 nm and 600-800 nm respectively. Here we are interested in perovskite oxide $KTaO_3$ which has many physical properties, such as ferroelectricity, electro-optic effect [3, 4]. Undoped $KTaO_3$ (lattice parameter a = 3.989 A°) is insulator with a relatively large band gap of around 3.8 eV [5]; hence it is transparent under visible light and the active region is in the ultraviolet range (wavelength < 400 nm). The high melting point of $KTaO_3$ also allow its applications at high operating temperature.

It is shown that $KTaO_3$ single crystal exhibit ultrafast photoelectric effect [6] when exposure to UV irradiation at room temperature. Angle-resolved photoemission spectroscopy (ARPES) study also shows that the increase in electron accumulation at the cleaved surface of insulating $KTaO_3$ samples can occur when the surfaces are exposed to intense synchrotron light (in ultraviolet range) [7]; similar effect was also observed at the surface of $SrTiO_3$ with electronic structure similar to $KTaO_3$ [8]. With interest in the observed change in surface property upon light exposure, here, we perform measurements of the $KTaO_3$ surface resistivity when the surfaces are exposed to sunlight and also controlled synchrotron light.

Materials and Methods

Sample preparation

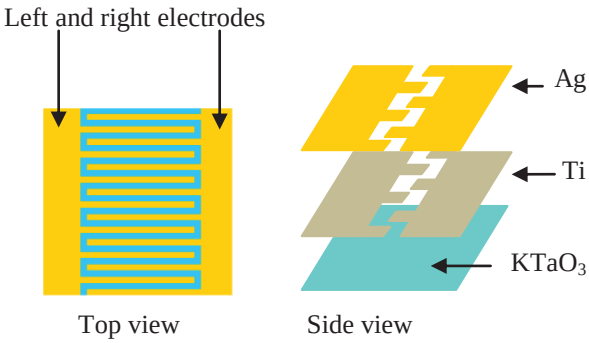

Figure 1. Electrode pattern of mixed silver and titanium metals on the $KTaO_3$ surface made by using lithography technique.

Potassium tantalum oxide samples ($KTaO_3$) measured in the work (Crystal Base Co., Japan) is

single crystal with (100) crystal orientation and 5 x 5 x 0.5 mm^3 in dimension. We make the pattern of electrode on the $KTaO_3$ surface by using lithography pattern. As shown in Fig. 1, titanium metal is first evaporated on the $KTaO_3$ and then silver metal is evaporated on top. Then, the top electrode is coated with the photoresist material (AZ). The electrode pattern is made by shining UV light through the lithography pattern mask. After washing out the photoresist material which gets exposed to UV light out, the electrode pattern on the $KTaO_3$ surface (see Fig. 1 (left) can then be obtained.

Resistance measurement

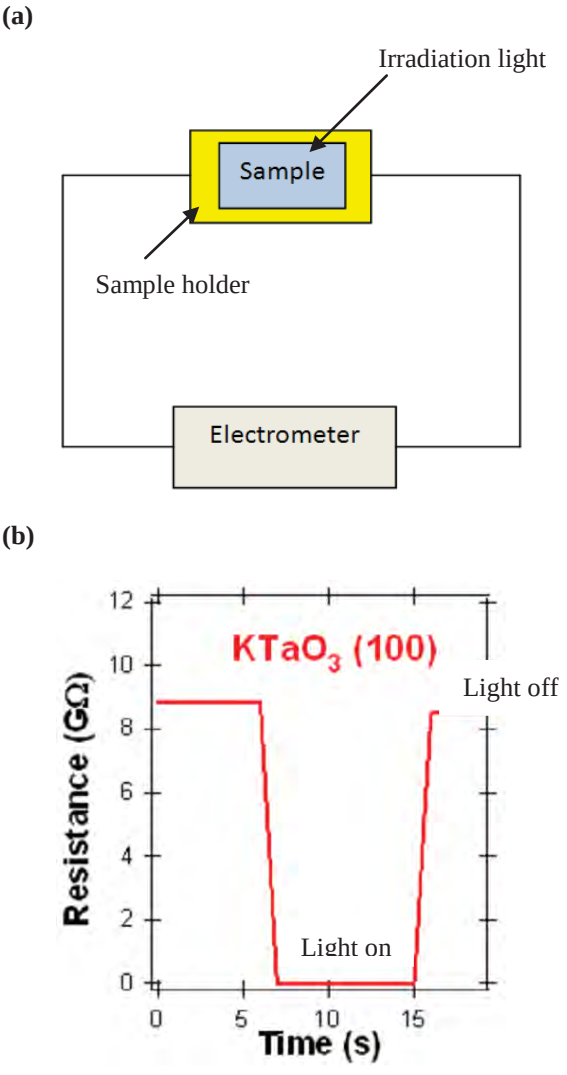

Figure 2. (a) Instrumental setup diagram for measuring resistance of samples in the range between 2 KΩ - 200 GΩ. (b) The resistance before and after light exposure on $KTaO_3$ when exposing to normal, unfocused sunlight**.**

To set up instrument to measure the difference in resistivity before and after light exposure, firstly, we design the sample holder for the $KTaO_3$ samples with the electrode pattern. As shown Fig. 2, the sample holder is connected to the Keithley electrometer model: 6514 which is capable of measuring the resistance upto 200 GΩ. With this setup, we first expose the sample surfaces of $KTaO_3$ with normal and unfocused sunlight and record the resistance as a function time. The samples are then exposed to focused sunlight by using a magnifying glass (14 cm in diameter). Next, the samples are then exposed to synchrotron light in a) the ultraviolet range and b) zero-order type (allowing all the frequencies to come through) at Beamline 3.2a, Synchrotron Light Research Institute, Thailand; note that the measurement under synchrotron light is performed at base pressure ~10^{-8} mbar.

Results and Discussion

We find that the conductivity of insulating $KTaO_3$ single crystals could change dramatically upon exposure of focused sunlight. When there was no light, the resistance of $KTaO_3$ was high in order of ~9 GΩ. As shown Fig. 2(a), when the sample was exposed to normal, unfocused sunlight, the resistance changed to approximately ~ 0.2 GΩ and when the sample was exposed to focused sunlight by using a magnifying glass, the resistance could become much lower in order of ~3 MΩ or approximately 3 orders of magnitude lower. This 3 orders of magnitude change is comparable to the ratio change in CdS and CdSe [1,2], indicating that KTaO3 can be used as high efficient light sensor. Note that this change in resistance upon exposure also happened very fast in time (faster than our instrumental limit) which is consistent with Ref. [6]. When the light is off, the resistance also changed back very fast at the slightly lower resistance (~8 GΩ) from the beginning.

We also perform a more controlled study by using the adjustable synchrotron light. The $KTaO_3$ resistance was observed to change in slower manner upon UV irradiation light at lower intensity. As shown Fig. 3(a), when there was no UV light (time = 0), the resistance of $KTaO_3$ was high in order of GΩ (~15 GΩ). Then we exposed the sample with UV light at photon energy of 60 eV; the photocurrent was set to 14 nA and the beam area was around 6 mm^2. The estimated intensity was 14 W/m^2. The exposure was repeatedly on 30 sec and off for another 30 sec during the measurement (see Fig. 3(a)). After the total time of around 32 mins, the resistance became saturated at the value ~0.5 GΩ or approximately 2 orders of magnitude lower.

The resistance changed more dramatically when exposed to synchrotron light at all frequency (zero order) as shown figure 3(b). When there was no light (at time = 0), the resistance of $KTaO_3$ was high in order of GΩ (~15 GΩ). At zero order, the photo current was at 10 μA whose intensity was estimated to be around $1x10^5$ W/m^2. The exposure on the sample was repeatedly on and off for 15 sec. The resistance

was first reduced quickly from 15 GΩ to 1.4 MΩ and then became saturated at the value around 1 MΩ or approximately 4 orders of magnitude lower. Note that when the light is off again completely, the resistance does not come back to the original value right away but increases slowly; the estimated time to come back to its original value is in order of many hours, which is consistent with ARPES data [7, 8]. Comparing with the measurement in ambient pressure (sunlight exposure), this slow change indicates that the air pressure has pronounced effect on the resistance change which is subject for further investigation.

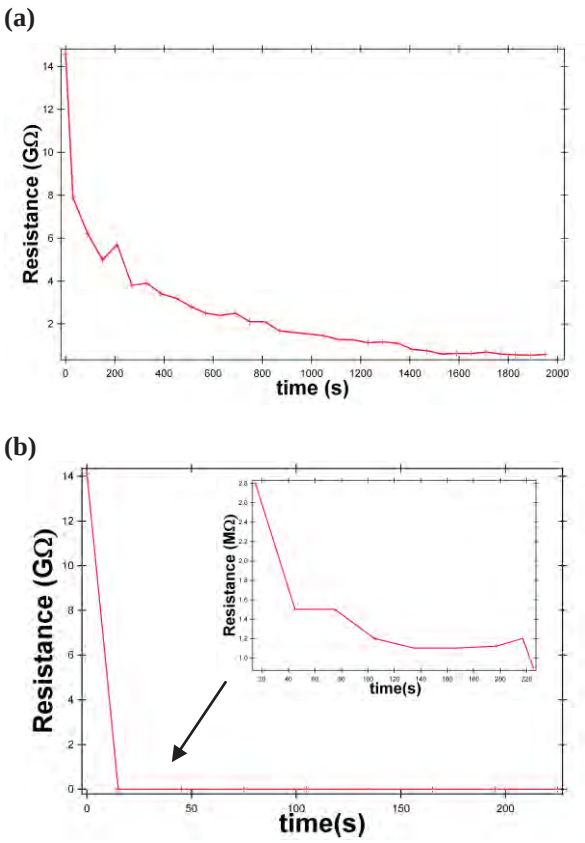

Figure 3. The resistance of $KTaO_3$ sample after exposed to (a) 60 eV synchrotron light with intensity ~ 14 W/m^2 and (b) zero order light with intensity ~ 10^5 W/m^2

Conclusions

The conductivity of $KTaO_3$ (100) could change dramatically upon exposure of focused sunlight. The resistance of $KTaO_3$ changes from in order of GΩ to MΩ or approximately 3 orders of magnitude lower. For UV synchrotron light at 60 eV, the resistance of $KTaO_3$ changed approximately 2 orders of magnitude lower. For zero order light, the resistance of $KTaO_3$ changes from in order of 10 GΩ to 1 MΩ or approximately 4 orders of magnitude lower. This results indicates that the $KTaO_3$ could be used as a high-efficiency light sensing device.

Acknowledgments

This work was supported by the Suranaree University of Technology, NANOTEC (Thailand), Thailand Research Fund and Office of Higher Education Commissions.

References

1. K. P. Mohanchandra, and J. Uchil, “Electrical properties of CdS and CdSe films deposited on vibrating substrates”, Journal of Applied Physics **84** (1998) 306.
2. S. Antohe, L. Ion, and V. A. Antohe, “The effect of the electron irradiation on the structural and electrical properties of a^{ii}-b^{vi} thin polycrystalline films”, Journal of Optoelectronics and Advanced Materials **5** (2003) 801 .
3. J. Toulouse, and R.K. Pattnaik, “Dielectric transparency induced by hetero-phase oscillations near the phase transition of relax or ferroelectrics", Physics Review Letter **79** (1997) 4677.
4. V. V. Laguta, M. D. Glinchuk, I. P. Bykov, A. Cremona, P. Galinetto, E. Giulotto, L. Jastrabik, and J. Rosa, “Light-induced defects in $KTaO_3$”, Journal of Applied Physics **93** (2003) 6056.
5. W.S. Baer, “Interband faraday rotation in some perovskite oxides, and rutile”, Journal Physics Chemistry of Solids **28** (1967) 677.
6. X. Jie, G. Er-Jia, J. Kui-Juan, L. Hui-Bin, H. Meng, W. Juan, and Y. Fang, “Ultraviolet Sensitive Ultrafast Photovoltaic Efect in Tilted $KTaO_3$ Single Crystals”, China Physics. Letter **27** (2010) 027202.
7. P. D. C. King, R. H. He, T. Eknapakul, P. Buaphet, S.-K. Mo, Y. Kaneko, S. Harashima, Y. Hikita, M. S. Bahramy, C. Bell, Z. Hussain, Y. Tokura, Z.-X. Shen, H. Y. Hwang, F. Baumberger, and W. Meevasana, “Subband structure of a two-dimensional electron gas formed at the polar surface of the strong spin-orbit perovskite $KTaO_3$”, Physics Review Letters **108** (2012) 117602.
8. W. Meevasana, P. D. C. King, R. H. He, S-K. Mo, M. Hashimoto, A. Tamai, P. Songsiriritthigul, F. Baumberger, and Z-X. Shen, “Creation and control of a two-dimensional electron liquid at the bare SrTiO3 surface”, Nature Materials **10** (2011) 114.